Alexander Volk, BSc

Electron Spin Resonance of Single ^{87}Rb Atoms Attached to Superfluid Helium Nanodroplets

MASTER THESIS

For obtaining the academic degree
Diplom-Ingenieur

Master Programme of
Technical Physics

Graz University of Technology

Supervisor: Univ.-Prof. Mag. Dr.rer.nat Wolfang E. Ernst
Co-Supervisor: Dipl.-Ing. Dr.techn. Markus Koch

Institute of Experimental Physics

Graz, May 2011

Danksagung

Mein besonderer Dank gilt meinem Betreuer Univ.-Prof. Mag. Dr.rer.nat. Wolfgang E. Ernst, der es mir ermöglichte meine Diplomarbeit am Institut für Experimentalphysik durchzuführen. Trotz seiner zahlreichen Termine fand er immer Zeit um mit mir über etwaige Probleme zu diskutieren und mich zu unterstützen.
Weiters möchte ich mich bei Dr. techn. Markus Koch bedanken, welcher mir als Co-Betreuer zur Seite stand. Nicht nur sein technisches Verständnis und seine Vorstellungen vom Laborbetrieb, sondern auch die oftmaligen Gespräche zu später Stunde im Labor, haben mir in vielerlei Hinsicht sehr geholfen.
Bei meinem Diplomarbeitspartner Johannes Poms bedanke ich mich für die gute Zusammenarbeit und seine Hilfe bei theoretischen Problemen.
Univ.-Prof. Laurentius Windholz danke ich für unzählige elektrische Durchführungen und seine Hilfsbereitschaft in fachlichen Fragen.
Rupert Maierhofer, Uwe Seidl und Werner Luttenberger haben alle von mir benötigten Bauteile nicht nur in bemerkenswerter Qualität gefertigt, sondern sind mir als AHS Absolventen auch bei den Planungen und technischen Zeichnungen oftmals eine große Hilfe gewesen.
Für seine große Hilfe bei der Erstellung der CAD Zeichnungen bedanke ich mich bei Günter Krois.
Bei allen anderen Arbeitskollegen und bei den Damen vom Sekretariat bedanke ich mich für für das kollegiale und freundschaftliche Arbeitsklima.
Michael Mayrhofer und Patrick Kraus danke ich für ihre Freundschaft und Unterstützung in außeruniversitären Fragen. Ich freue mich schon sehr auf unsere weitere Zusammenarbeit.
Ohne Gernot Kapper, meinen treuen Labor- und Übungspartner wäre ich wohl noch nicht einmal am Anfang meiner Diplomarbeit.

Mein besonderer Dank gilt aber meinen Eltern Beatrix und Franz, die mir mein Studium nicht nur finanziell ermöglicht, sondern mich auch sonst immer auf alle erdenkliche Art unterstützt haben. Auch meine Schwester Alena stand mir in arbeitsintensiven Zeiten immer unterstützend zur Seite.

Kurzfassung

Superfluide Helium Nanotröpfchen bieten mit ihren sehr niedrigen Temperaturen von 0.38 K einen perfekten Nanokryostaten für die spektroskopische Untersuchung von einzelnen Atomen, Molekülen, oder Clustern. An von Tropfen aufgesammelten Alkalimetallen (vorwiegend ^{85}Rb) durchgeführte Elektronen Spin Resonanz (ESR), zeigt eine Störung der Elektronenwellenfunktion $\psi(r)$ der Dotieratome. Diese Störung wird als Erhöhung der Hyperfeinkonstante a_{HFS} um ca. 400 ppm modelliert. Um Spin Labeling Experimente durchzuführen, bei denen für ESR normalerweise unzugängliche Spezies mit Hilfe der gut bekannten Alkalimetallatomen als Spin Labels untersucht werden, ist es vorteilhaft die Sensitivität der Methode zu erhöhen.
Hierzu wird in einem ersten Ansatz ^{87}Rb im Zuge dieser Arbeit untersucht, da dieses Isotop eine größere Hyperfeinkonstante ($a_{\mathrm{HFS}} \approx 3417\,\mathrm{MHz}$) aufweist. Nach einer kurzen Beschreibung der zugrundeliegenden Theorie, werden einige wichtige apparative Verbesserungen dokumentiert. Weiters werden die ersten ESR Spektra von ^{87}Rb Monomeren auf Helium Tröpfchen zusammen mit den zugehörigen Änderungen von a_{HFS} präsentiert. Die Ergebnisse werde mit jenen von ^{85}Rb verglichen, und einige wichtige Eigenschaften der Linien, welche nun aufgrund der höheren Sensitivität erstmals zugänglich sind, werden diskutiert.
Abschließend wird eine neue Auswertemethode für a_{HFS} vorgestellt, bei welcher die Änderung von a_{HFS} anstatt für vollständige ESR Spektra nun für einzelne ESR Linien berechnet wird. Die Kombination der erhaltenen Ergebnisse mit einer detailierten Analyse der Linienform, welche Gegenstand derzeitiger Arbeit ist, könnte den Zugang zur Tropfengrößenverteilung erstmals durch ESR Messungen ermöglichen.

Abstract

Superfluid helium nanodroplets with their very low temperature of 0.38 K provide a perfect nanocryostat for the spectroscopic investigation of isolated atoms, molecules, or clusters. Electron spin resonance (ESR) spectroscopy performed on alkali-metal atoms (mainly ^{85}Rb) which were picked up by these droplets, showed a perturbation of the dopant's electron wavefunction $\psi(r)$. This perturbation is modelled as an increase of the hyperfine constant a_{HFS} by ≈ 400 ppm. In order to perfom spin labeling experiments, where ESR silent species are investigated by using a well known alkali-metal atom as spin label, it is advantageous to enhance the sensitivity of the method.
As a first approach, ^{87}Rb is investigated in this work because of its larger hyperfine coupling constant ($a_{\mathrm{HFS}} \approx 3417$ MHz). After a short description of the theoretical background, some important experimental improvements are documented. Further on, the first ESR spectra of ^{87}Rb monomeres on helium nanodroplets are presented along with the corresponding changes of a_{HFS}. The results are compared to those of ^{85}Rb and some important line features, which are now accessible due to the higher sensitivity, are discussed.
Finally, a new evaluation method for a_{HFS} is introduced, where the change of a_{HFS} is calculated for single ESR lines instead of using a whole ESR spectrum. The combination of the obtained results with detailed line shape analysis, which is the subject of current work, may grant access to the droplet size distribution from ESR measurements for the first time.

Deutsche Fassung:
Beschluss der Curricula-Kommission für Bachelor-, Master- und Diplomstudien vom 10.11.2008
Genehmigung des Senates am 1.12.2008

EIDESSTATTLICHE ERKLÄRUNG

Ich erkläre an Eides statt, dass ich die vorliegende Arbeit selbstständig verfasst, andere als die angegebenen Quellen/Hilfsmittel nicht benutzt, und die den benutzten Quellen wörtlich und inhaltlich entnommene Stellen als solche kenntlich gemacht habe.

Graz, am ……. ……..
(Unterschrift)

Englische Fassung:

STATUTORY DECLARATION

I declare that I have authored this thesis independently, that I have not used other than the declared sources / resources, and that I have explicitly marked all material which has been quoted either literally or by content from the used sources.

……. ……..
date (signature)

Contents

List of Figures

List of Tables

Introduction

Superfluid helium nanodroplets provide several desirable properties for high resolution spectroscopy because of their extremely low temperature of 0.38 K [19] combined with their weak interaction with dopants [49] (see Sec. 1.1). On the other hand, electron spin resonance (ESR) with hyperfine resolution is sensitive to changes in the electronic structure of atoms or molecules (see Sec. 1.3), which are in this case induced by the perturbing helium droplet.
In 2008 these two methods were combined for the first time at the Institute of Experimental Physics at Graz University of Technology. For this purpose, a conventional molecular beam apparatus was reconstructed into a helium droplet beam apparatus by Markus Koch during his PhD thesis [27]. A detailed description of the measurement setup can be found in Ref. [30]. Extensive drawings of the apparatus were provided by Johannes Lanzersdorfer in his master thesis [32].
The results of ESR investigations of the alkali-metal atoms ^{39}K and ^{85}Rb attached to helium droplets, show a change of the hyperfine constant a_{HFS} by about 300-400 ppm, induced by interactions with the droplet [27, 28, 30]. A direct correlation between the change of a_{HFS} and the size of the helium droplets has been shown [29]. Further on, the measuring of Rabi oscillations proved coherent ESR transitions [27, 28].
However, one future goal is to investigate ESR-silent species, thereby using the alkali-metal atoms as spin labels. As the relative hyperfine structure parameter change is expected to be similar, this method will be more sensitive for elements or isotopes with large energy differences between the involved hyperfine niveaus. Taking account of this fact, the isotope ^{87}Rb is used for the experiments in this work, because of its high value of $a_{\mathrm{HFS}} \approx 3417$ MHz.
As a second goal, the investigation of ^{52}Cr has been prepared by Martin Ratschek through the design of an electron-bombardment evaporation source [46, 47].

Chapter 1 gives a short overview of the theoretic concepts, while Chapter 2 deals with the experimental setup and its upgrades. The design of a new laser setup as well as improvements of the vacuum conditions as a result of the installation of bake out facilities and a new cryo pump, enhanced the signal to noise ratios.
The expected high sensitivity could be verified as described in the first part of Chapter 3, corresponding to the publication "**^{87}Rb Electron Spin Resonance on Helium**

Nanodroplets: The Influence of Optical Pumping", by Alexander Volk, Johannes Poms, Markus Koch, and Wolfgang E. Ernst, that was accepted as part of the "J. Peter Toennies Festschrift" in *The Journal of Physical Chemistry A*, and will appear soon [50]. This high sensitivity allows to observe the droplet size distribution by a detailed analysis of the lineshape of single ESR transitions. Therefore, an extensive list of all ESR measurements is compiled using a new method, where a_{HFS} is evaluated on the basis of single lines.

1. Theoretical Background

1.1. Superfluid Helium Nanodroplets

In spectroscopy, there is a huge amount of techniques to simplify the obtained spectra and to enhance resolution. As an example the reduction of rotational and vibrational energies of molecules leads to a high simplification of the emitted spectra and can be achieved with seeded supersonic beams [14]. On the other hand, transient species (atoms, free radicals, or ions) can be investigated by use of cryogenic matrix isolation. However, there are also problems occuring with these techniques, resulting in a broadening of the spectral lines [2, 49].
Since the first experimental realisation of a beam consisting of superfluid helium nanodroplets (He_N) in 1961 by Becker et al. [6], they were object to many investigations. Being transparent for light from the vacuum ultraviolet to the far infrared made them also interesting for spectroscopic experiments, especially in the last decade. Their special properties have been reviewed for example by Toennies and Vilesov [48, 49] or Callegari and Ernst [10]. In brief, the reason for the widespread application of He_N lies in the superfluidity at very low temperatures (see Fig. 1.1). This behaviour offers various advantages over the methods mentioned above because the attached species (called dopants) can move freely in the droplet, but still are well localized because of the finite size of the He_N. Further on, the interaction between the dopants and the surrounding He atoms is very low, although high enough to cool the dopant to its electronic ground state [49].

1.1.1. Helium Droplet Beam Production and Properties

The production of helium droplets and their properties have been described in several books (e.g. [37, 40]), and the following concepts are taken from these monographs.
A He droplet beam can be produced via free jet supersonic expansion of gaseous helium through the small orifice of a cooled nozzle. This corresponds to an adiabatic expansion along isentropes from the gaseous phase to the liquid phase (see Fig. 1.1). The formation of He_N can be described using either a macroscopic or a microscopic model.
In the first case one speaks of supersaturation when the liquid phase boundary is crossed by the isentrope and formation of droplets is a consequence of the return to equilibrium. On the other hand, the microscopic model assigns droplet growth to the condensation of

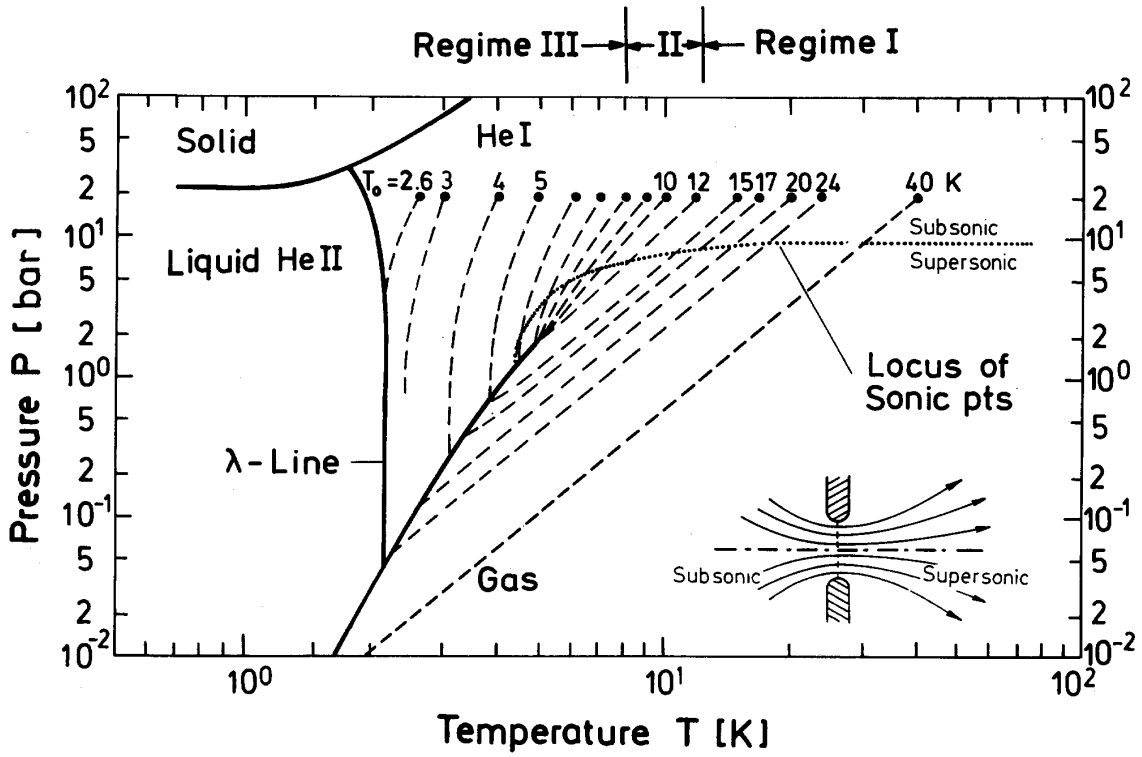

Figure 1.1.: Phase diagram of ^{4}He. There is no tripple point, but a superfluid phase (Liquid HeII) at low temperatures and pressures. Adiabatic expansions follow isentropes, indicated by dashed lines. Their starting points lie at a stagnation pressure of 20 bar and between 2.6 to 40 K. On the top axis the partitioning of the phase diagram into three regimes is indicated. (taken from [9])

He atoms on oligomeres. The process starts with the formation of dimers, which themselves are created by three body collisions in the vicinity of the nozzle orifice. As collisions between the particles decrease drastically, the growth of the droplets has finished at a distance of approximately 1000 orifice diameters [49].
Note that the starting point of the isentrope can lie in one of the three regimes shown in the P-T diagram (see Fig. 1.1). Ideal gas behaviour for the expansion as assumed above, can only be expected for starting temperatures corresponding to regime I, which is true for measurements presented in this work. Conditions are different for regime III, where the helium is already fluid inside the nozzle. One cannot speak of a supersonic expansion in this case, but droplets result from a break up of the liquid jet streaming out of the orifice [49]. Regime II can be seen as an intermediate regime where an exact description is difficult due to density fluctuations [9].
After the period of growth, the ^{4}He droplets cool down to a final temperature of 0.38(1) K [19]

by evaporation of single atoms. The pickup of a different species leads to further evaporation. This process, combined with the very large heat capacity of He_N, makes the droplet a perfect nanocryostat of constant temperature for any dopant [49].

Droplet Size and Velocity

Experimental results for the size distribution of He_N were obtained by either embedding electrons and then deflecting the charged droplets in an electric field, or by crossing the beam with a second beam consisting of heavy rare gases, which leads to mass correlated deflection angles [20, 25, 33]. The obtained data is well reflected by the Knuth model and the power model [24, 26, 27]. To give an example, the power model is shown in Eqn. 1.1. The values for the four parameters k_1-k_4 are taken from [27].

$$\bar{N} = k_1 p_0^{k_2} T_0^{k_3} d^{k_4} \tag{1.1}$$
$$k_1 = 4(7) \cdot 10^5,\ k_2 = 0.97(9),\ k_3 = -3.88(25),\ k_4 = 2.0(1.1)$$

One can see that the mean number of atoms $\bar{N}$ in the droplet depends on the source temperature T_0 in K, the source stagnation pressure p_0 in bar, and the diameter of the nozzle orifice d in μm. For all measurements presented in this work the pressure was fixed to $p_0 = 50\,\text{bar}$, and T_0 varied from 12-23 K. With a given d of $5\,\mu$m, this led to droplet sizes between 1000 to 30000 atoms per droplet.
The size distribution was measured by Lewerenz [33] and for more different size conditions by Harms et al. [20]. They found a log-normal distribution:

$$P(N) = \frac{1}{\sqrt{2\pi} N \delta} \exp\left[-\frac{(\ln N - \mu)^2}{2\delta^2}\right] \tag{1.2}$$

P gives the probability to find a droplet consisting of N atoms. If the distribution parameters μ and δ are known, $\bar{N}$ can be calculated with Eqn. 1.3.

$$\bar{N} = \exp\left(\mu + \frac{\delta^2}{2}\right) \tag{1.3}$$

For the full width at half maximum (FWHM) of the distribution one finds:

$$\Delta N_{1/2} = \exp\left(\mu - \delta^2 + \delta\sqrt{2\ \ln 2}\right) - \exp\left(\mu - \delta^2 - \delta\sqrt{2\ \ln 2}\right) \tag{1.4}$$

Of course the radius of the droplet is directly connected to the number of atoms contained, and for ^{4}He Eqn. 1.5 holds [49].

$$R_0 = 2.22 N^{\frac{1}{3}} \mathring{A} \tag{1.5}$$

The velocity of the droplets can be calculated (Eqn. 1.6) assuming ideal gas behaviour and is in good agreement with experimental results (Ref.[9]).

$$v = \sqrt{2(H_0 - H_\lambda)} \qquad (1.6)$$
$$H_0 = \frac{5}{2} k_\mathrm{B} T_0$$

H_0 and H_λ are the enthalpies at the starting point of the isentrope and at the lambda point (Fig. 1.1), k_B is the Boltzman constant and T_0 the source temperature. Values for H_λ are tabulated in [36] and v lies in the range of 200 to 400 ms^{-1} [49].

Pickup

The first pickup of SF_6 by argon clusters was reported by Gough et al. in 1985 [16]. Later experiments have shown, that helium droplets are well suited for picking up any species they collide with [49].
Depending on the chemical potential μ of the dopant (which corresponds to the binding energy between dopant and droplet), one can distinguish between "heliophilic" and "heliophobic" species [49]. Heliophobic alkali metals like the investigated ^{87}Rb, have positive values for μ and reside at the surface of the droplet, where a dimple is formed [1]. Almost all other species like e.g. xenon, on the other hand, have a negative chemical potential leading to localisation inside the droplet, which is also predicted by density functional theory (DFT) [13].
In most cases of experimental realisation, the $\mathrm{He_N}$ beam flies through a pickup cell, where the dopant is provided at pressures between $4 \cdot 10^{-5}$ and $1 \cdot 10^{-5}$ mbar. For ^{87}Rb as well as for other solid species, this means that the cell has to be heated. It turned out that for Rb 85°C are the optimum temperature for the pickup cell in the experiment [27].
At the pickup, the dopant transfers kinetic and internal energy to the droplet which leads to evaporation of helium atoms. As a consequence, the temperature stays constant as described in Sec. 1.1.1. For ^{4}He this leads to evaporation of approximately 1600 atoms for 1 eV of transfered energy, which is equivalent to a heat of evaporation of 7 K or the energy of one photon at 5 cm^{-1} per He atom [49].
The probability for a droplet to pick up a certain number of particles can be modelled by a Poisson distribution [34, 49]:

$$I_k = I_{k,0} \frac{(\alpha L)^k}{k!} \exp(-\alpha L) \qquad (1.7)$$

with k the number of particles picked up, L the length of the pickup cell and α a factor containing information about the cross section, the particle density and the relative velocity of scattering gas and beam. This model neglects the droplet size distribution as well as the evaporation of He atoms during the pickup process and assumes that the constant

pickup cross section is equal to the geometrical cross section.
For the special case of alkali metal pickup the description is slightly different, because in case of multiple pickup only high-spin configurations can stay at the droplet, while low spin states desorb due to an energy release because of spin saturation [39, 51]. In this case the probability distribution in Eqn. 1.8 (taken from [51]) models the experimental data near the optimum pickup pressure better than a pure Poisson distribution.

$$P(l) = \frac{l+1}{2^l}\left[\frac{1}{4} + \mathcal{P}(l) - \frac{1}{4}\sum_{k=0}^{l+1}\mathcal{P}(k)\right] \tag{1.8}$$

Here l is the number of atoms picked up and $\mathcal{P}$ the Poisson distribution with the mean number of collisions $\langle k \rangle$. Note that the droplet shrinking and the droplet size distribution are still neglected in this newer model.

1.2. Rubidium as investigated element

The discovery of rubidium (Rb) is a result of flame spectroscopy, performed by Kirchhoff and Eberhard in 1861 [23]. Rb is an alkali element and situated in the 5th row of the periodic table. The atomic number is 37.
There are only two isotopes of interest for our experiments, namely ^{85}Rb and ^{87}Rb. ^{85}Rb with a natural abundance of 72.17 % is stable, while ^{87}Rb (27.83 %) has a half-life time of $4.88 \cdot 10^{10}$ years [35]. Some important physical properties are given in Tab. 1.1.

Table 1.1.: Important physical properties of Rb.

Property	^{85}Rb	^{87}Rb	Unit	Ref.
atomic weight	85.47		g/mol	[35]
density (at 25 °C)	1.53		g/cm^3	[35]
melting point	39.48		°C	[35]
boiling point	688		°C	[35]
electronic D_1 transition	12578.950		cm^{-1}	[45]
electronic D_2 transition	12816.545		cm^{-1}	[45]
electron g-value g_e $^2S_{1/2}$	2.00233113		–	[3]
electron g-value g_e $^2P_{1/2}$	0.666		–	[3]
electron g-value g_e $^2P_{3/2}$	1.334		–	[3]
nuclear spin I	5/2	3/2	–	[35]
nuclear g-value $g_I \cdot 10^4$	-2.93640 [1]	-9.95141 [1]	–	[3]
hyperfine coupling constant a_{hfs}	1011.910813	3417.34131	MHz	[3]

The vapor pressure of Rb in dependence of the temperature T can be calculated using

$$\log_{10}(p) = 5.006 + A + BT^{-1} \tag{1.9}$$

with the pressure p given in Pascal. The values of A and B change at the melting point, being $A = 4.857$, $B = -4215\,\mathrm{K}$ for solid Rb and $A = 4.312$, $B = -4040\,\mathrm{K}$ for liquid Rb respectively [35].

[1] The given values for g_I are true for $\mu_I = g_I \mu_B m_I$, with μ_I the magnetic moment of the nucleus, μ_B the Bohr magneton and m_I the nuclear magnetic quantum number (see Sec. 1.3 for further information). This definition is always used in this work. However, there exists also a different definition in literature, using a nuclear magneton μ_N instead of μ_B, which leads to different values for g_I.

1.3. Electron Spin Resonance

Electron spin resonance (ESR) of a sample in a test tube was experimentally observed for the first time in 1944 by Zavoiski in Russia [53]. Since then, the physical concept as well as the spectroscopic application of ESR have been described in many textbooks (see e.g. Refs. [4, 17, 52]).
Essential for every measurement is the magnetic moment of electron spins called $\boldsymbol{\mu}_\mathrm{s}$. As this moment adds up to zero for antiparallel spins, unpaired electrons are required in the sample. For alkali-metal atoms the spin quantum number S is 1/2 and the spin magnetic quantum numbers are $m_\mathrm{s} = \pm 1/2$ (see Tab. 1.2). The two possible alignments of $\boldsymbol{\mu}_\mathrm{s}$ with an external field $\boldsymbol{B}_0$ ($\boldsymbol{B}_0 = (0, 0, B_0)$), namely parallel (spin down, $m_\mathrm{s} = -1/2$) or antiparallel (spin up, $m_\mathrm{s} = +1/2$), exhibit different energies [4, 17]

$$E_{\mathrm{m_s}} = g_\mathrm{e} \mu_B m_\mathrm{s} B_0 \tag{1.10}$$

The Landé g-factor for electrons g_e is approximately 2.002 (see Tab. 1.1).
$\mu_\mathrm{B} = \frac{e\hbar}{2m_\mathrm{e}} \approx 9.274 \cdot 10^{-24}\,\mathrm{J/T} \approx 13.996\,\mathrm{GHz/T}$ is the Bohr magneton, containing the elementar electric charge e and the electron mass m_e. Transitions between the two energy states can be induced for unpaired electrons by application of a resonant magnetic field if the frequency ν satisfies the relation [4, 17]

$$\Delta E = g_\mathrm{e} \mu_B B_0 = h\nu \tag{1.11}$$

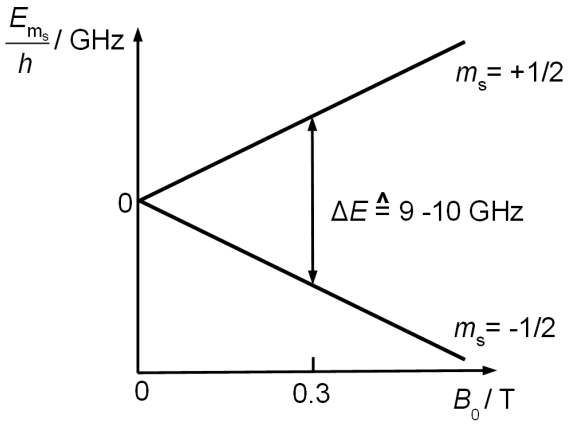

Figure 1.2.: Spin dependent energy level shift for a free electron in a magnetic field B_0 according to Eqn. 1.10. The resonance frequency for a transition (see Eqn. 1.11) is indicated for $B_0 = 0.3\,\mathrm{T}$.

Typical values of ν lie in the range of 9-10 GHz and therefore belong to the X band of

the microwave (MW) region of the electromagnetic spectrum [4, 17]. Resonance can be obtained by either scanning B_0 or ν. In most cases a MW cavity is used to amplify the MW field, which makes it necessary to keep the value of ν fixed. In ordinary ESR spectrometers the change of absorption of the MW radiation by the probe is measured as an indicator for resonance. B_0 normally is in the range of 0.3 T and provided by an electromagnet [4, 17]. The energy level shift for a free electron in a magnetic field and a possible transition at $B_0 = 0.3\,\mathrm{T}$ are depicted in Fig. 1.2.

1.3.1. Molecular Beam Magnetic Resonance

Already in 1938, the group of Rabi observed magnetic resonance in molecular beams [43, 44]. The problem of the low particle density in the beam was overcome by an indirect detection technique. Two inhomogeneous magnetic fields A and B were used as state selectors. Particles with a certain magnetic moment $\boldsymbol{\mu}$ were deflected by A and then in the opposite direction by B, depending on their spatial alignment, so that they could reach the detector. If a resonant MW field C was applied between A and B, the spatial alignment of the magnetic moments changed, leading to different deflection of the corresponding particles by B, so that they missed the detector.

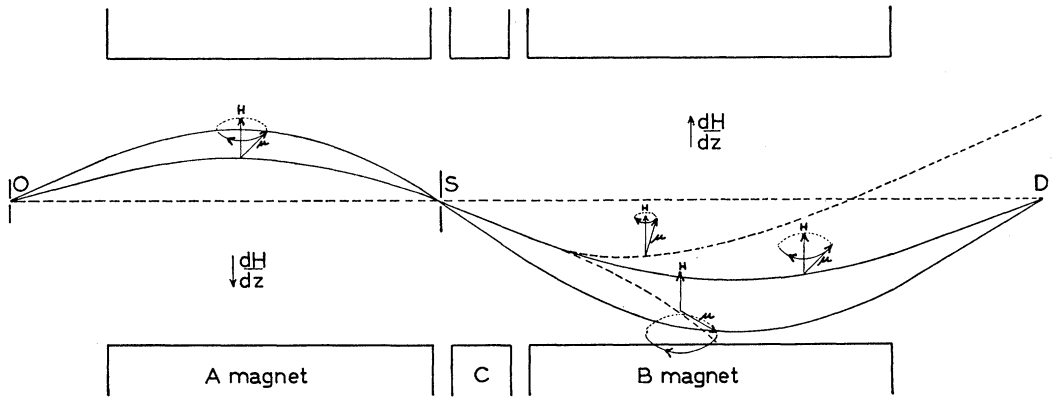

Figure 1.3.: Schematic setup of the Breit–Rabi apparatus. The gradients of the two inhomogeneous magnetic fields A and B point in opposite direction. O denotes the source of molecules, D is the detector and S is a collimating slit. If no resonant MW field C is applied, the molecules are deflected by A and B by the same amount but in opposite direction (solid curves). If the magnetic moment $\boldsymbol{\mu}$ is changed by help of C, the molecules can not reach the detector any more (dotted curves). In addition, the precession of the magnetic moments around the quantisation axes (direction of H) is indicated. (taken from [43])

Nowadays it is possible to replace the inhomogeneous magnetic fields A an B by homogeneous magnetic fields, and to select certain energy states of the particles with single frequency laser light [14]. The key to this method are single frequency lasers, which deliver radiation of a well defined energy, and therefore can adress hyperfine energy states $E(\boldsymbol{\mu}_s,\boldsymbol{\mu}_I)$, with $\boldsymbol{\mu}_I$ the magnetic moment of the nucleus. Note that this is only true for free atoms, as for species attached to He_N the energy levels are not resolved due to a perturbation by the droplet (see Sec. 1.3.3).
The low particle density is compensated by high photon density. Before explaining the pump and probe process itself, which is done in Sec. 1.3.3, it is therefore necessary to deal with the energy level diagram of ^{87}Rb.

1.3.2. Fine and Hyperfine Splitting of ^{87}Rb

As described in various books e.g. [17, 21], the angular momentum $\boldsymbol{L}$ and the spin angular momentum $\boldsymbol{S}$ of the electron, as well as the angular momentum of the nucleus $\boldsymbol{I}$ influence the atomic energy levels by interacting with each other. In this section a brief description of the coupling of atomic momenta shall be given for ^{87}Rb. In closed shells, the magnetic moments of the electrons add up to zero so that only the valence electron is of interest. Tab. 1.2 lists the basic quantum numbers (QNs) for the ^{87}Rb ground state.

Table 1.2.: Basic quantum numbers for ^{87}Rb in the electronic ground state.

name	character	possible values
principal QN	n	5
orbital angular momentum QN	L	0,1,...,$n-1$
orbital magnetic QN	m_L	0,$\pm$1,... $\pm L$
spin QN	S	1/2
spin magnetic QN	m_S	$\pm 1/2$
total angular momentum QN	J	$\lvert L \pm S \rvert$
total magnetic QN	m_J	$0, \pm 1, ..., \pm J$
nuclear QN	I	3/2
nuclear magnetic QN	m_I	$I, I-1, ..., -I$
total angular momentum QN including nuclear spin	F	$J+I, J+I-1, ..., \lvert J-I \rvert$
total magnetic QN including nuclear spin	m_F	$F, F-1, ..., -F$

Fine splitting

$\boldsymbol{L}$ and $\boldsymbol{S}$ couple to the total angular momentum of the electron $\boldsymbol{J} = \boldsymbol{L} + \boldsymbol{S}$, resulting in the QNs J and m_J (see Tab. 1.2). The total magnetic moment of the electron $\boldsymbol{\mu}_\mathrm{J}$ can then be calculated using

$$\boldsymbol{\mu}_\mathrm{J} = -\frac{g_\mathrm{J}\mu_\mathrm{B}}{\hbar}\boldsymbol{J} \tag{1.12}$$

For $L = 0$, the Landé factor g_J can be approximated by g_e (see Tab. 1.1).
The relative motion of electron and nucleus to each other induces a magnetic field at the position of the electron. As a result of the interaction between $\boldsymbol{\mu}_\mathrm{J}$ and this field, one can observe the so called fine splitting, leading to the well known dublett structure in the spectrum of elements with one valence electron (D_1 and D_2 transitions see Tab. 1.1) [17, 21].

Hyperfine Splitting

Hyperfine splitting results from the additional interaction with the angular momentum of the nucleus $\boldsymbol{I}$. The corresponding quantum numbers I and m_I can be found in Tab. 1.2. As a result one obtains the total angular momentum including nuclear spin called $\boldsymbol{F} = \boldsymbol{J} + \boldsymbol{I}$ and therefore two further quantum numbers namely F and m_F (see Tab. 1.2). The electron causes a magnetic field $\boldsymbol{B}_\mathrm{J}$ at the position of the nucleus, and the possible alignments of the nuclear magnetic moments $\boldsymbol{\mu}_\mathrm{I}$ with respect to that field cause an additional shift of the atomic energy levels by the amount of

$$E_\mathrm{HFS} = -\boldsymbol{\mu}_\mathrm{I}\boldsymbol{B}_\mathrm{J} = \frac{a_\mathrm{HFS}}{2}\left[F(F+1) - I(I+1) - J(J+1)\right] \tag{1.13}$$

a_HFS is called hyperfine constant and can be calculated by

$$a_\mathrm{HFS} = \frac{g_\mathrm{I}\mu_\mathrm{B}B_\mathrm{J}}{\sqrt{J(J+1)}} \tag{1.14}$$

using the values given in Tab. 1.1 for g_I. The energy splitting ΔE_HFS between two vicinal hyperfine states with the QNs F and $F+1$ can be determined using

$$\Delta E_\mathrm{HFS} = E_\mathrm{HFS,F+1} - E_\mathrm{HFS,F} = a_\mathrm{HFS}(F+1) \tag{1.15}$$

For s- electrons $\boldsymbol{B}_\mathrm{J}$ is strongly determined by the non vanishing value of $|\psi(0)|^2$, i.e. the propability that the electron is at the position of the nucleus. The interaction between

the magnetic moments of electron and nucleus is called Fermi contact interaction in this case and the hyperfine constant can be expressed by

$$a_{\mathrm{HFS}} = \frac{2}{3}\mu_0 g_{\mathrm{e}} g_{\mathrm{I}} \mu_{\mathrm{B}}^2 |\psi(0)|^2 \tag{1.16}$$

with the vacuum permeability $\mu_0 = 4\pi \cdot 10^{-7}\,\mathrm{Vs/(Am)}$ [17, 21].
It is important to note, that all states corresponding to a certain value of F are still $2F+1$ fold degenerate because of the different possible values for m_{F}. If an external magnetic field $\boldsymbol{B}_0$ is applied, these states split according to the possible alignments of $\boldsymbol{\mu}_{\mathrm{J}}$ with $\boldsymbol{B}_0$ (see Fig. 1.5). This is true for weak fields, the so called Zeeman regime, while there is a decoupling of $\boldsymbol{\mu}_{\mathrm{I}}$ and $\boldsymbol{\mu}_{\mathrm{J}}$ in the Paschen–Back regime for strong $\boldsymbol{B}_0$ [17, 21].

Zeeman splitting and Paschen–Back effect

In the Zeeman regime the degenerated energy levels seperate and shift linear with increasing $\boldsymbol{B}_0$. The additional energy $E_{\mathrm{HFS,Ze}}$ is given by

$$E_{\mathrm{HFS,Ze}} = g_{\mathrm{F}} \mu_{\mathrm{B}} B_0 m_{\mathrm{F}} \tag{1.17}$$

$$g_{\mathrm{F}} = g_{\mathrm{J}} \frac{F(F+1) + J(J+1) - I(I+1)}{2F(F+1)} - g_{\mathrm{I}} \frac{F(F+1) + I(I+1) - J(J+1)}{2F(F+1)} \tag{1.18}$$

This system is treated in the $|J, I, F, m_{\mathrm{F}}\rangle$ basis. Transitions between the energy levels of the electric ground state follow the selection rules of electric dipole transitions, i.e. $\Delta F = 0, \pm 1$ and $\Delta m_{\mathrm{F}} = 0, \pm 1$. Electronic excitation requires $\Delta L = \pm 1$ [17, 21].
For the Paschen–Back regime, F and m_{F} are not good QNs any more. The reason for this is the decoupling of $\boldsymbol{I}$ and $\boldsymbol{J}$, arising from the fact that the interaction between $\boldsymbol{B}_0$ and $\boldsymbol{\mu}_{\mathrm{J}}$ is stronger than between $\boldsymbol{\mu}_{\mathrm{J}}$ and $\boldsymbol{\mu}_{\mathrm{I}}$. Different energy levels can be deduced from the possible alignments of $\boldsymbol{\mu}_{\mathrm{J}}$ with $\boldsymbol{B}_0$ and $\boldsymbol{\mu}_{\mathrm{I}}$ with $\boldsymbol{B}_{\mathrm{J}}$. The energy level shifts $E_{\mathrm{HFS,PB}}$ (see Eqn. 1.19) contain these interactions in the first two parts, while the third part reflects the interaction of $\boldsymbol{\mu}_{\mathrm{I}}$ with $\boldsymbol{B}_0$ [17, 21].

$$E_{\mathrm{HFS,PB}} = g_{\mathrm{J}} \mu_{\mathrm{B}} B_0 m_{\mathrm{J}} + a_{\mathrm{HFS}} m_{\mathrm{I}} m_{\mathrm{J}} - g_{\mathrm{I}} \mu_{\mathrm{B}} B_0 m_{\mathrm{I}} \tag{1.19}$$

It is obvious from Eqn. 1.19 that the quantum numbers m_{J} and m_{I} are well suited to describe the different levels and so the $|J, I, m_{\mathrm{J}}, m_{\mathrm{I}}\rangle$ basis is used to treat a system in this regime. The selection rules are $\Delta m_{\mathrm{J}} = \pm 1$, $\Delta m_{\mathrm{I}} = 0$ for ESR transitions (which is equivalent to $\Delta m_{\mathrm{S}} = \pm 1$ for $L = 0$), and $\Delta m_{\mathrm{I}} = \pm 1$, $\Delta m_{\mathrm{J}} = 0$ for nuclear magnetic resonance (NMR) transitions [17, 21].

Note that the third part in Eqn. 1.19 dominates at ultra-high $\boldsymbol{B}_0$, when the external field is stronger than $\boldsymbol{B}_\mathrm{J}$, which is in the range of 1 T [17, 21].
In Fig. 1.4 this is summarised and the energy level diagram is depicted for the $^2\mathrm{S}_{1/2}$ and $^2\mathrm{P}_{1/2}$ states of ^{87}Rb.

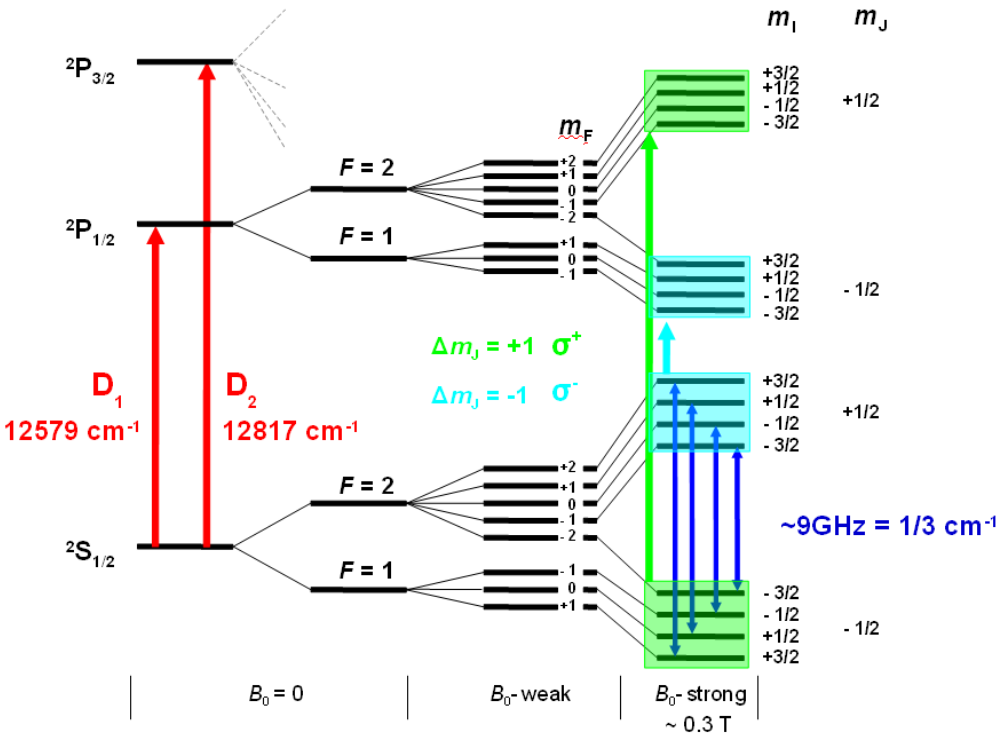

Figure 1.4.: Energy level diagram for $^2\mathrm{S}_{1/2}$ and $^2\mathrm{P}_{1/2}$ states of ^{87}Rb. The levels are labeled with the valid quantum numbers in each case. B_0-weak marks the Zeeman regime, while B_0-strong indicates the Paschen–Back regime. Electronic D_1 and D_2 transitions are plotted with red lines. The blue lines indicate the ESR transition observed in the experiments of this work. Further on, the light blue and green boxes with corresponding lines show the transitions that occur for optical pumping when the effect of MCD is exploited (see Sec. 1.3.3). Note that the energy differences are not to scale, which can also be seen by the given numerical values.

The Breit–Rabi Formula

While the distance between two adjacent hyperfine energy levels rises linearly with $\boldsymbol{B}_0$ in each of the two regimes discussed above, this is not true for the intermediate regime. Here one can obtain the energy levels by diagonalisation of the corresponding Hamiltonian [21].

$$\mathcal{H}_{\mathrm{HFS}} = \mathcal{H}_{\mathrm{MD}} + \mathcal{H}_{\mathrm{mag}} \tag{1.20}$$

The first term corresponds to the hyperfine part of the magnetic dipole interaction and the second term represents the interaction of atomic magnetic moments with the external field. Using the vector operators of the respective angular momenta, one obtains the following expressions:

$$\mathcal{H}_{\mathrm{MD}} = a_{\mathrm{HFS}} \frac{\hat{\boldsymbol{I}}\hat{\boldsymbol{J}}}{\hbar^2} \tag{1.21}$$

$$\mathcal{H}_{\mathrm{mag}} = \frac{\mu_{\mathrm{B}}}{\hbar} \left(g_{\mathrm{J}} \hat{J}_{\mathrm{z}} - g_{\mathrm{I}} \hat{I}_{\mathrm{z}} \right) B_{\mathrm{z}} \tag{1.22}$$

$\mathcal{H}_{\mathrm{MD}}$ is diagonal in the $|JI; Fm_{\mathrm{F}}\rangle$ basis and $\mathcal{H}_{\mathrm{mag}}$ has off-diagonal elements given by the so called Clebsch–Gordan coefficients. However, it can be diagonalised in the same basis, to solve the problem [21].
An analytical solution for the energy levels for the special case of $L = 0$ is delivered by the Breit–Rabi formula (Eqn. 1.23 - 1.25) [7, 31], which simplifies the calculations.

$$E_{\mathrm{HFS,BR}} = -\frac{\Delta E_{\mathrm{HFS}}}{2(2I+1)} + g_{\mathrm{I}}\mu_{\mathrm{B}} B_0 m_{\mathrm{F}} \pm \frac{\Delta E_{\mathrm{HFS}}}{2} \sqrt{1 + \frac{4m_{\mathrm{F}}}{2I+1} x + x^2} \tag{1.23}$$

$$\text{for } |m_{\mathrm{F}}| < I + \frac{1}{2}$$

$$E_{\mathrm{HFS,BR}} = -\frac{\Delta E_{\mathrm{HFS}}}{2(2I+1)} \pm g_{\mathrm{I}}\mu_{\mathrm{B}} B_0 m_{\mathrm{F}} + \frac{\Delta E_{\mathrm{HFS}}}{2}(1 \pm x) \tag{1.24}$$

$$\text{for } |m_{\mathrm{F}}| = I + \frac{1}{2}$$

$$\text{with } x = \frac{(g_{\mathrm{J}} - g_{\mathrm{I}})\mu_{\mathrm{B}} B_0}{\Delta E_{\mathrm{HFS}}} \tag{1.25}$$

Fig. 1.5 shows the calculated hyperfine level energies of the $^2\mathrm{S}_{1/2}$ state of $^{87}\mathrm{Rb}$, for typical external fields applied in the measurements.

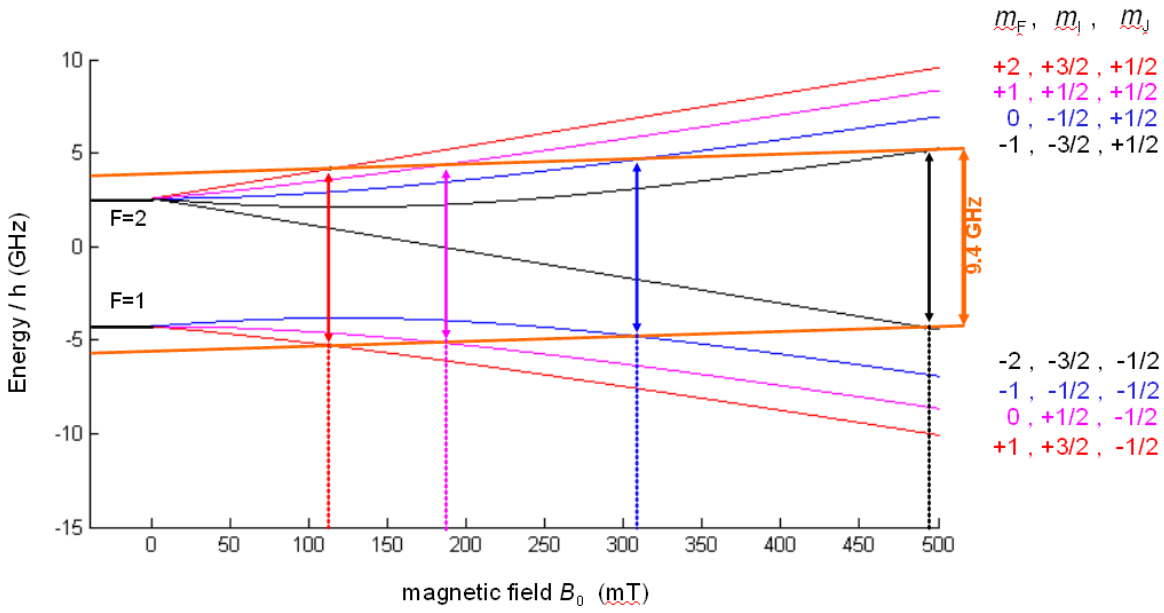

Figure 1.5.: Hyperfine energy level shifts for the $^2S_{1/2}$ state of ^{87}Rb calculated with the Breit–Rabi formula (Eqn. 1.23 - 1.25). For $B_0 = 0$ the degenerated F-levels are indicated. One can see linear behaviour for weak magnetic fields (Zeeman regime), where the energy levels can be labeled using the QN m_F. For strong fields (Paschen–Back regime) the QNs m_I and m_J have to be used. ESR transitions according to a MW frequency of 9.4 GHz are also displayed.

1.3.3. Optically Detected Magnetic Resonance and Magnetic Circular Dichroism

As mentioned above, it is possible for free atoms, to investigate energy changes of certain hyperfine levels when selecting these levels by means of optical pumping [14, 17, 18]. A single frequency laser, excites electrons of a certain substate to a higher state, from where they can relax again. This relaxation process follows certain transition propabilities, so that not all of the electrons will relax to their initial groundstate. It is therefore possible to deplete the initial groundstate if the atom undergoes multiple pumping cycles. The pump laser corresponds to the A-field of the Breit–Rabi apparatus (see Sec. 1.3.1).

Instead of the B-field, a weaker probe beam is used. Only if the initially depleted substate has been reoccupied, there will be an excitation by the probe beam, connected to laser induced fluorescence (LIF). For long spin relaxation times it is assured that the depleted state is only occupied if a transition between the substates has been induced by the MW-field C. Detailed information about this method, called optically detected magnetic resonance (ODMR) can be found in Ref. [12].
For helium droplets doped with Rb, the D_1 line is approximately $100\,\mathrm{cm}^{-1}$ broad [8], while the investigated ESR transitions lie in the range of $1/3\,\mathrm{cm}^{-1}$ (Fig. 1.4). This makes it impossible to selectively address hyperfine substates of the $^2S_{1/2}$ state with a single frequency laser as discussed for the free atoms. Instead, the effect of magnetic circular dichroism (MCD) is exploited, i.e. the dependence of selection rules on the polarisation of the laser light. $\sigma^{\pm}$ polarisation of the incident laser light leads to transitions between hyperfine states with $\Delta m_\mathrm{F} = \pm 1$ (see Fig. 1.4). This causes depletion of either all $^2S_{1/2}$ $m_J = -1/2$ or $m_J = +1/2$ states via excitation in the $^2P_{1/2}$ $m_J = \pm 1/2$ levels. The laser light of the probe laser has to have the same polarisation as for the pump laser, so that the detection principle stays the same as for free atoms, despite the fact that more hyperfine substates are involved in pump and probe process. Certain ESR transitions between $^2S_{1/2}$ sublevels can then be selected by scanning the external field $\boldsymbol{B}_0$, so that the applied MW-field with fixed frequency is resonant with only one transition at the same time.
The experimental setup for optically detected magnetic resonance of alkali-metal atoms on helium droplets can be seen in Fig. 2.1.

2. Experimental Setup

The experimental setup has been described in great detail by Markus Koch in his PhD thesis and corresponding publications [27, 28, 30]. Additional information regarding the design of the apparatus, including extensive CAD drawings, can be found in the diploma thesis of Johannes Lanzersdorfer [32]. Adaptations of the setup, like the implementation of a pickup cell for gas pickup and the installation of a quadrupole mass spectrometer, have been made and documented by Martin Ratschek in his master thesis [46].
In this chapter only a brief summary of the measuring principles relevant for this work shall be given. Further on, changes in the experimental setup are explained and documented. Besides the design of a new laser setup and the installation of supplementary components like anti-reflection coated windows and a flow box, some efforts were made to improve vacuum conditions. Bake out facilities and a new cryo pump in the pickup chamber, in combination with the installation of a foreline molecular sieve and a nitrogen ventilation system, led to good results.
Additional changes made during the time dedicated to this work, may be described in the master thesis of Johannes Poms [41].

2.1. Basic measuring principles

In order to observe hyperfine resolved ESR of alkali-metal atoms attached to He_N, the technique of ODMR (see Sec. 1.3) has been applied. Figure 2.1 illustrates the most important steps in the experiment starting from left:
Droplets (light blue) consisting of $2000 - 20000$ He atoms are produced via supersonic free jet expansion from a cold nozzle (see 1.1). After they have passed a skimmer (grey), they fly through a pickup cell where Rb atoms (red) are picked up. The pickup process is optimized for monomer pickup.
After the pickup, the droplets enter the field of an electromagnet (poles indicated by red and green cuboids). Spin up ($\uparrow$) and spin down ($\downarrow$) states of the Rb atoms each occur with a probability close to 1/2. In fact, the occupation numbers $N_{1,2}$ follow the Boltzmann distribution (Eqn. 2.1), but the spin temperature is not cooled by the droplet, which can be seen from long spin lifetimes (see Ref. [5]). In combination with the small energy differences between the involved states, equal population is a justifiable approximation.

$$\frac{N_2}{N_1} \propto \exp\left(-\frac{E_2 - E_1}{k_B T}\right) \tag{2.1}$$

Note that there are also Rb atoms effusing from the cell, which have not been picked up by a droplet. These particles will be referred to as free atoms in the following.
Because of the magnetic field, the degenerate energy levels split according to Fig. 1.4. Now it is possible to induce a difference in state occupation by means of optical pumping with σ- polarized laser light (exploiting the effect of MCD see Sec. 1.3.3). In case of Fig. 2.1, all Rb atoms are in a $\downarrow$ state after the intersection with the pump laser beam. This means that the pump laser addresses all spin up ($\uparrow$)(!) states, thereby pumping them into the other state. If there is no interaction with a resonant MW-field, the Rb atoms stay in this state until the droplets cross the probe laser beam, which is due to the long spin relaxation times (see Ref. [5]).
This laser beam has the same polarisation as the pump beam, therefore also addresses the same spin states. As this states have been emptied before, no laser induced fluorescence (LIF) can be observed. However, if a microwave (MW) field (yellow) is applied between the two laser beams, a spin flip is induced as soon as the field is in resonance with the corresponding transition energy (see Sec. 1.3). In that case, the probe beam can excite atoms and their relaxation fluorescence can be detected with a photomultiplier tube. Both laser beams are created by the same Ti:Al_2O_3 laser (Coherent, Inc., 899-01 series) and cross the apparatus perpendicular to the droplet beam axis.
To apply the MW field, a MW cavity is placed in the course of the beam. The droplets can pass through two orifices in the cavity and "see" the field inside. For all measurements presented in this work, the MW frequency is kept constant at 9442 ± 1 MHz, using a MW synthesizer (HP83620A). Adaptations are only made to compensate for small, thermal induced size variations of the cavity, so that the field is always in resonance with the cavity. The MW field is switched on and off periodically and a trigger signal is transmitted to a homemade counter. Also connected to the counter is a (single photon sensitive) photomultiplier tube, detecting LIF which is collected at the intersection of probe laser and droplet beam. The counter assigns the signals to on and off periods and the two resulting data sets are transmitted to a computer, where they are processed by LabView programs. This method makes it possible to subtract the background signal, which is recorded during periods where the MW field is switched off, from the total signal.
To obtain resonance of MW field for different hyperfine transitions, the magnetic field (B_0) is scanned. Therefore it is necessary to manually adjust the voltage applied to the electromagnet in a first step, so that B_0 is close to the value where a transition can be expected. In the second step, small changes of B_0 are induced by two scanning coils, whose applied voltage can be controlled by LabView programs combined with a controllable power supply. Investigations were made to determine the stability of the magnetic field and results will be presented in the work of Johannes Poms [41].

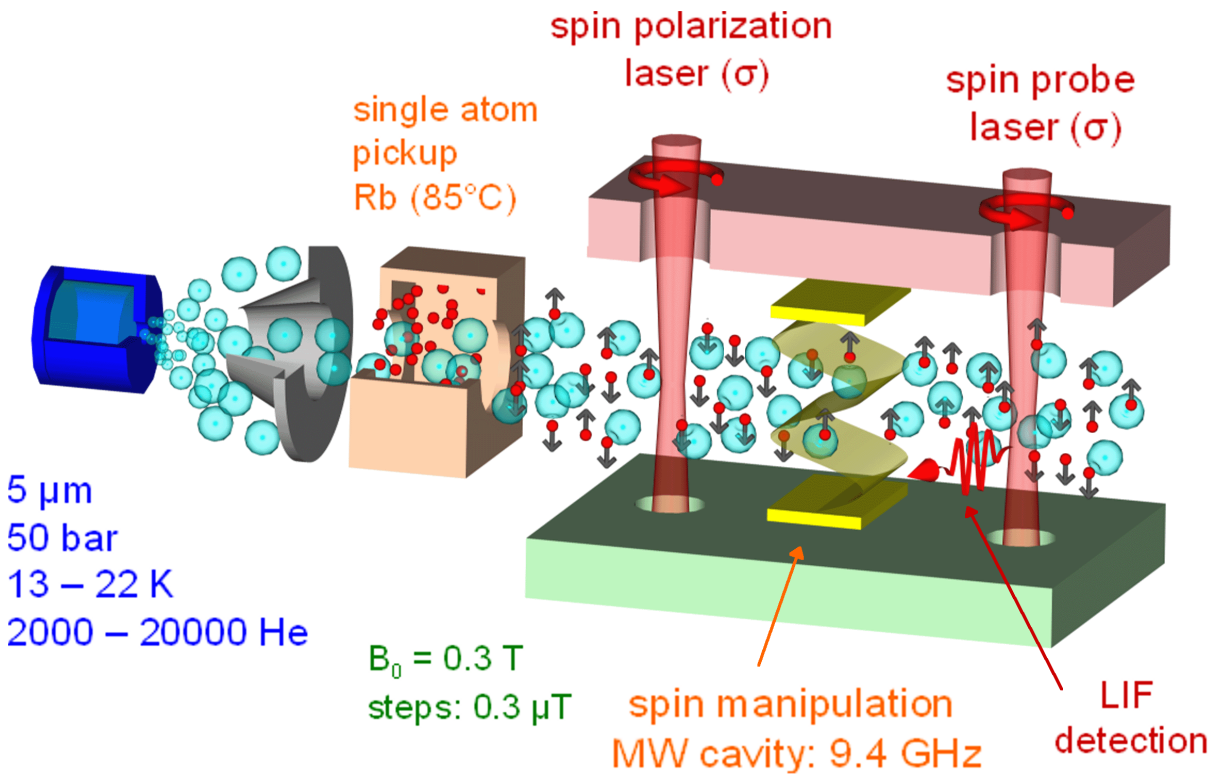

Figure 2.1.: Setup for optically detected magnetic resonance of alkali-metal atoms on helium droplets. (taken from [27])

B_0 is determined by an NMR magnetometer (Drusch RMN2). The magnetometer head is placed slightly above the droplet beam so that the exact field at the position of the droplets cannot be measured, as the homogeneity of B_0 is not perfect. In order to overcome this problem, a second laser is tuned to the D1 line's hyperfine component under investigation of the free atoms. For this purpose a grating stabilized, single mode diode laser (Toptica Photonics AG, TA 100) is used. The corresponding peak in the ESR spectra, resulting from the free atoms, can be set to the value for B_0 where transitions for free atoms are predicted by the Breit–Rabi formula (see Eqn. 1.23 - 1.25). Using this marker to calculate magnetic field shifts between free atoms and Rb atoms attached to droplets, makes it possible to evaluate changes of the hyperfine coupling constant a_{HFS} as explained in Sec. 3.1.
More detailed information about the laser setup will be given in Sec. 2.2.
The apparatus is divided into three vacuum chambers, which are connected along the droplet beam axis, but can be separated by gate valves. In the first chamber the helium source is located, the second chamber contains the pickup cells (one for alkali-metal pickup

and one for gas pickup) and in the third chamber the measurements take place. Also situated in the third chamber is a Langmuir–Taylor detector, with which the alkali-metal pickup can be monitored. Further on, a quadrupole mass spectrometer (QMS) is attached to the end of the third chamber, also separated by a gate valve and pumped separately. Detailed information regarding the pressures are given in Sec. 2.3, where all modifications of the vacuum system are documented.

2.2. Adaptation of the Laser Setup

Since the last description of the pump-probe laser setup in Ref. [27], various changes have been made and shall be documented in this section. Fig. 2.2 shows a schematic drawing of the new setup, while Tab. 2.1 gives further information about the distances between single components.

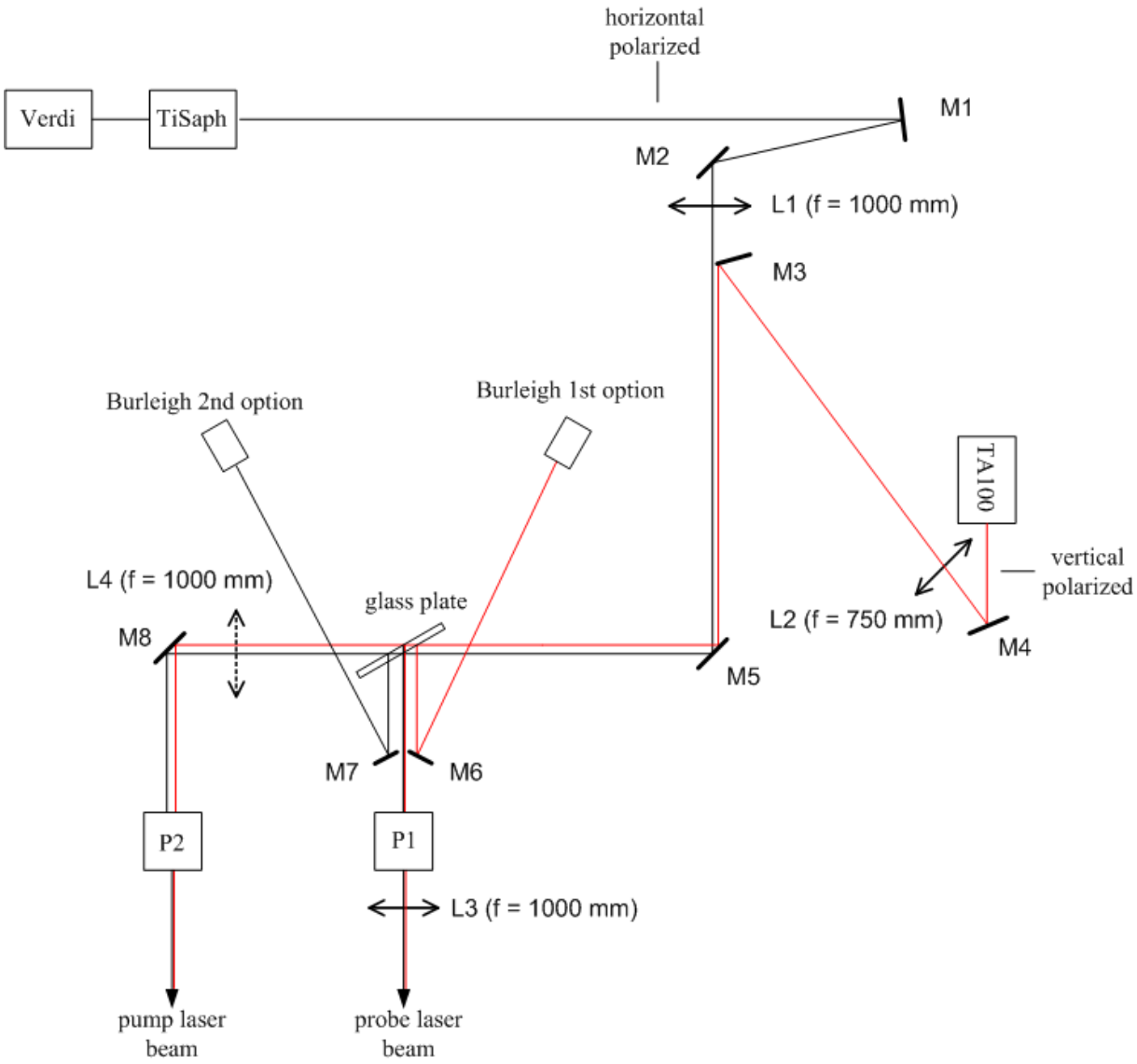

Figure 2.2.: New pump-probe laser setup. Verdi...diode-pumped solid-state frequency-doubled Nd:YVO_4 pump laser, TiSaph...cw Ti:Al_2O_3 ring laser, TA100...grating stabilized diode laser with a tapered amplifier, Burleigh...wavemeter, P1-2...Pockels cells, L1-4...lenses, M1-8...mirrors.

Table 2.1.: Distances d between components of the pump-probe laser setup. The denotation corresponds to Fig. 2.2.

segment	d / mm
TiSaph–M1	765
M1–M2	280
M2–L1	50
L1–M5	450
TA100–M4	230
M4–L2	115
L2–M3	420
M3–M5	360
M5–glassplate	800
glassplate–P1	195
P1–L3	130
glassplate–M6	100
glassplate–M7	100
M6–Burleigh$_1$	290
M7–Burleigh$_2$	290
glassplate–L4	55
glassplate–M8	250
M8–P2	150
P1–intersection with He_N beam	1340
P2–intersection with He_N beam	1340

The Ti:Al_2O_3 (TiSaph) ring laser is now pumped by a compact diode-pumped solid-state frequency-doubled Neodymium Vanadate (Nd:YVO_4) laser (Coherent, Inc., Verdi dual FAP laser system) with single-frequency output at 532 nm. This laser is situated in cluster lab II, as well as all other optical components. The output power of the Verdi undergoes only small fluctuations, leading to very stable operating conditions for the TiSaph ring laser.

The horizontal and vertical alignment of the TiSaph laser beam can be adjusted with two mirrors (M1, M2). A small divergence of the beam is corrected with lens L1. The adjustment of M3, M4 and L2 follows the same principles for the diode laser. As indicated in Fig. 2.2, M3 is positioned very close to the beam of the TiSaph laser, so that the two laser beams are almost parallel and very close to each other after this mirror.

At the glass plate, each beam is split into three parts. While most of the intensity can pass right through, reflections occur at the front and rear side of the plate. In the right alignment the front side reflection of the TiSaph laser overlaps with the rear side reflection of the diode laser, so that both parts can be focused with L3. These beams serve as probe

beams for atoms attached to He_N and for free atoms. The two other reflections are used to determine the corresponding laser wavelengths with a wavemeter (Burleigh).
The pump beams are generated by the non reflected parts of the original laser beams. Because of different divergencies of the two laser beams, L4 is only necessary to focus the diode laser beam and can be omitted during measuring with the TiSaph laser (see Sec. 2.2.1). It is placed in such a way that the laser beam focus lies before the intersection with the droplet beam, meaning that there is a larger interaction volume but still high laser intensity at the intersection point. As said before, L4 is omitted while measuring with the TiSaph laser, because the high output power of the laser combined with an additional collimation would lead to a very high energy density at the intersection point with the He_N beam. This would reduce the amplitude of the obtained ESR signals because of beam depletion [11]. Recording ESR spectra with different output powers p of the TiSaph laser and calculation of the corresponding signal to noise ratios showed that the best results are obtained for $p_{\mathrm{pump}} = 2.2\,\mathrm{W}$ and $p_{\mathrm{probe}} = 240\,\mathrm{mW}$. The diode laser is always operated at maximum power, which gives $p_{\mathrm{pump_D}} = 137\,\mathrm{mW}$ and $p_{\mathrm{probe_D}} = 1.2\,\mathrm{mW}$.
As explained before (see Sec. [ODMR]), the effect of MCD is exploited. It is possible to obtain σ^+, σ^- or linearly polarized laser light for pump and probe beam, by switching the Pockels cells with the voltages given in Tab. 2.2. Note that the signs of the voltages depend on the mounting direction of the Pockels cells.

Table 2.2.: Voltages V applied to the Pockels cells P1 and P2 to get the desired laser light polarization for pump- and probe beam.

Polarization	V_{P1} / kV	V_{P2} / kV
σ^+	-2.7	$+2.7$
lin	0.0	0.0
σ^-	$+2.7$	-2.7

2.2.1. Measuring procedure

As only one of the two lasers is resonant with an ESR transition at the same time (because the magnetic field is scanned), but both produce stray light, it turned out to be a good method to use the TiSaph laser and the diode laser alternatingly. This appreciably increases the signal to noise ratios.
In case of ^{87}Rb, the scanning times between the points where one of the lasers is in resonance with a transition, are in the range of several seconds. It is therefore possible to start a measuring cycle with one of the two lasers being blocked while the magnetic field is scanned. After the first ESR peak has been recorded, the second laser is unblocked and

the first one is blocked. It depends on the scanning direction of the magnetic field and the expected relative positions of the two peaks, whether the TiSaph or the diode laser has to be blocked first. L4 is inserted when the diode laser is unblocked and removed otherwise (see above).

2.2.2. Additional Upgrades of the Optical Assembly

Anti Reflection Coated Windows

Plane glass plates, like the windows, where the laser beams enter the molecular beam apparatus, are working as Fabry–Perot interferometers. Multiple beam interference leads to a frequency dependence of the transmitted intensity I_{T} which can be described by the corresponding Airy formula[14]:

$$I_{\mathrm{T}} = I_0 \frac{(1-R)^2}{(1-R)^2 + 4R\sin^2(\phi/2)} \tag{2.2}$$

The phase difference ϕ between two interfering light beams in the glass plate is connected to the path difference Δs and the laser frequency ν (c being the speed of light):

$$\phi = \frac{2\pi\nu\Delta s}{c} \tag{2.3}$$

Frequency oscillations are possible, because the laser is not in a single mode operation modus. This leads to intensity fluctuations after the beam has crossed the windows of the vacuum chamber, thereby causing also fluctuations in the LIF signal. It is obvious from Eqn. 2.2, that the influence of ν on I_{T} can be reduced by using windows with very low reflectivity R. The new quarz windows in use are coated on both sides with an anti-reflection coating (Qioptic Photonics, NIR ARB2) for the laser frequencies used. This coated windows have a typical reflectivity of $< 0.35\,\%$ for wavelengths in the range of 725-1050 nm and solved the problem.

Flow Box

Initially the high photon density inside the TiSaph laser's ring resonator led to a soiling of the laser mirrors with dust particles, which in turn caused a noticeable drop of the output intensity. This problem was overcome by the installation of a flow box , i.e. a filter box that provides a laminar flow of cleaned air, above the whole optical setup.
All the changes mentioned above led to great improvements concerning laser stability and intensity. Further improvements could be expected by overlapping the TiSaph and the diode laser beams with a beamsplitter. This would in principle be possible as the polarization planes of the two beams are perpendicular to each other (see Fig. 2.2).

2.3. Adaptation of the Vacuum Setup

High vacuum is necessary in this experiment mainly because of two reasons. The first reason is, that the mean free path $\bar{l}$ of a particle is inverse proportional to the pressure p in the apparatus (see Eqn. 2.4 [22]). Other variables influencing the value of $\bar{l}$ are the temperature T of the residual gas and the diameter d of the particles. This is also true for He_N droplets flying through the apparatus. Naturally, deflection of droplets because of collisions as well as extensive droplet shrinking due to particle pickup, are highly undesirable effects. The only way to avoid such unwanted interactions, is to increase the mean free path by working under high vacuum conditions. An estimation of the necessary vacuum pressure, so that the mean free path lies in the range of the length of the apparatus, is made in Sec. A.1.1. It shows that for large droplets a pressure of approximately $4.4{\cdot}10^{-8}$ mbar would be required, which is already in the ultra-high vacuum region.

$$\bar{l} = \frac{k_B \cdot T}{\sqrt{2}\pi p d^2} \tag{2.4}$$

The second reason to work under high vacuum conditions is the minimisation of possible interactions between the Rb atoms on the droplets and other, unwanted dopants. With the aim of perfoming spin labeling experiments, the absence of elements or molecules with large dipole moment is required. Recent measurements showed a large pickup of H_2O molecules by He_N [46]. These molecules may dominate over effects that are expected to be seen in spin labeling experiments.
Therefore, some efforts were taken to reduce the quantity of water in the pick up chamber. As standard approaches, bake out facilites were installed as well as a cryo pump in the pickup chamber.

2.3.1. Bake Out Facilities

For the bake out of the pick up chamber two heating tapes (Atek, HTS, 240V/624W) were fixed along the edges of the chamber. This assures efficient heating not only of the outer chamber walls, but also the inner ones between source- and pickup- as well as between pickup- and measurement chamber. As power supply a variable transformer (Gebr. Ruhstrat, Typ RTK, Nr.2443/9) and an isolation transformer (L. Wimberger KG, Typ ETW 00-3) are used. The total electrical power is measured between the two transformers with a commercial powermeter (Globaltronics GmbH & Co.KG, GT-PM-02).
The intent is to reach a stable maximum temperature of about 80 °C to prevent any damage of the elastomer sealings. To monitor the temperature, three K-type thermocouples are mounted at different positions of the chamber wall, the corresponding temperatures are referred to as T_1, T_2, and T_3.
T_1 is measured at a side flange (on the right side when looking in the droplet beam direc-

tion), on which two further flanges with electrical feedthroughs are mounted. T_2 and T_3 are both taken from the upper wall, T_2 from a position in the middle and T_3 from near the gate valve, between source and pick up chamber (see Ref. [32] for detailed drawings). For the following measurements a total electrical power of appoximately 420 W was applied, which can be realised with the variable transformer tuned to 65 % of the maximum voltage. The time evolution of the temperatures and the pressure in the pickup chamber p_c is depicted in Fig. 2.3 and 2.4 for heating and cooling periods respectively. One can see that the temperature T_x of the chamber reached a value of 79 °C after approximately 25 hours of heating and then stayed constant. T_3 shows a higher value, but is not really reflecting the temperature of the chamber wall. It rather corresponds to the temperature of the heating band due to a direct thermal contact. This can especially be seen in Fig. 2.4, where T_3 drops of very quickly. For the heating period, the temperature behaviour was fitted using

$$T(t) = T_\mathrm{max} - (T_\mathrm{max} - T_\mathrm{0,h}) \cdot \exp\left(\frac{-t}{\tau_\mathrm{h}}\right) \tag{2.5}$$

for each data set. A suitable model for the cooling period is given by

$$T(t) = T_\mathrm{min} + (T_\mathrm{0,c} - T_\mathrm{min}) \cdot \exp\left(\frac{-t}{\tau_\mathrm{c}}\right) \tag{2.6}$$

The time evolution of p_c was fitted for the cooling period using

$$p(T) = p_\mathrm{min} + p_1 \cdot \exp\left(\frac{-t}{\tau_\mathrm{pc1}}\right) + p_2 \cdot \exp\left(\frac{-t}{\tau_\mathrm{pc2}}\right) \tag{2.7}$$

as a guide to the eye, while no fit was made for the heating period due to the lack of a suitable model. The resulting fit parameters are given in Tab. 2.3.

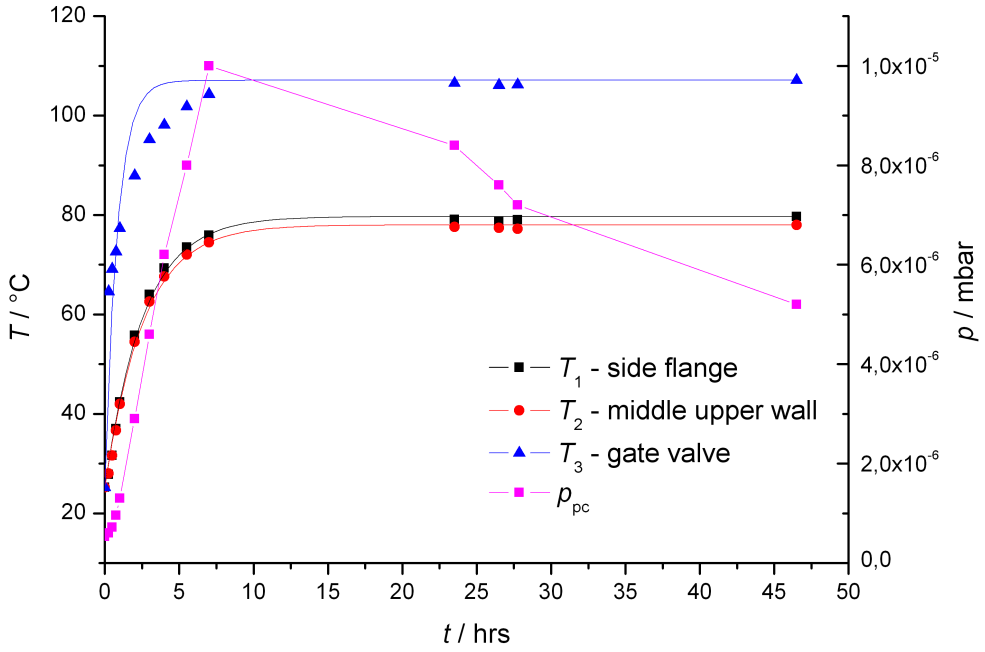

Figure 2.3.: Time evolution of the chamber wall temperature and of the pressure in the pickup chamber during heating for bake out. The temperature was measured at three different positions. T_3 is too high due to a measurement error (see text for further information). The three temperature data sets were each fitted using $T(t) = T_{\max} - (T_{\max} - T_{0,\mathrm{h}}) \cdot \exp\left(\frac{-t}{\tau_\mathrm{h}}\right)$. p_pc rises with temperature mainly because of the desorption of H_2O molecules. After a constant wall temperature has been reached, p_pc starts sinking because the effective amount of water in the chamber decreases. The data points for p_pc were not fitted due to the lack of a suitable model.

Bake out facilities were also installed at the measurement chamber. As two heating tapes of the same type as for the pickup chamber are used, all statements are also true for the measurement chamber, except for longer time scales because of the larger size and therefore higher mass of this chamber.
After the bake out of both chambers a reasonable decrease of water pickup by the He_N could be seen in QMS measurements, which leads to the assumption that the higher pressure during the bake out process reflects mainly the desorption of H_2O molecules.
As a consequence of the heating process an additional problem occured. For pressures in the pick up- and in the measurement chamber of arround $2 \cdot 10^{-7}$ mbar, it is a simple and cheap method to seal the electrical feedthroughs with epoxy adhesive. When baking out the system, this can lead to troubles, because the adhesive softens at about 60 °C, which then causes leaks. The problem was resolved by a redesign of all affected flanges, now

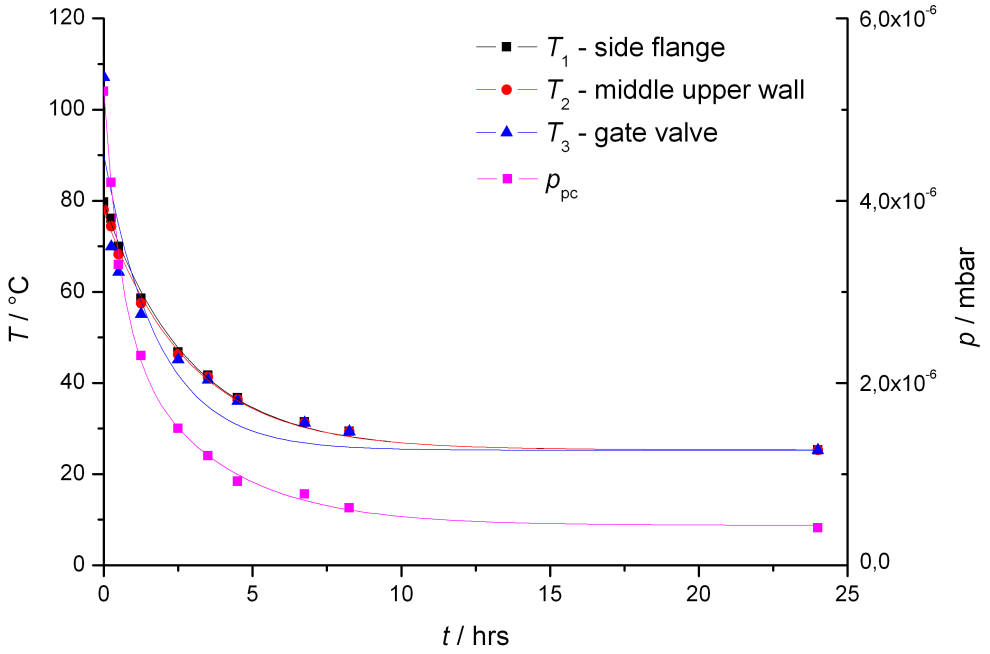

Figure 2.4.: Time evolution of the chamber wall temperature and of the pressure in the pickup chamber during the cooling period of the bake out process. The temperature was measured at three different positions. T_3 deviates from the expected behaviour for the first three data points due to a measurement error (see text for further information). The three temperature data sets were each fitted using $T(t) = T_{\min} + (T_{0,\mathrm{c}} - T_{\min}) \cdot \exp\left(\frac{-t}{\tau_\mathrm{c}}\right)$. p_pc falls with temperature mainly because adsorption of H_2O molecules becomes more likely than desorption for cold chamber walls. The data points for p_pc were fitted using $p(T) = p_{\min} + p_1 \cdot \exp\left(\frac{-t}{\tau_{\mathrm{pc}1}}\right) + p_2 \cdot \exp\left(\frac{-t}{\tau_{\mathrm{pc}2}}\right)$ as a guide to the eye.

using commercial weldable feedthroughs.
Further improvements could be achieved by heating to higher temperatures. This would be possible after removal of all sealings in exchange for new viton sealings, which can bear temperatures up to 200 °C [22]. Note that a copper cable between the pickup cell and the chamber wall assures thermal contact, mainly to cool the cell after its heating cartridges have been turned off. For high temperatures of the chamber walls during the bake out process, it will therefore be necessary to cool the pickup cell, in order to save Rb. This can be done by passing the cable through the wall and installing an external water cooling system.

Table 2.3.: Fit parameters for temperatures and pressures recorded during bake out corresponding to Eqns. 2.5-2.7. The error of the last digit is given in parentheses.

data set	parameter	value	unit
$T_1/T_2/T_3$ heating	$T_{0,\mathrm{h}}$	25.2	°C
T_1 heating	$T_{\max}$	79.7(4)	°C
T_1 heating	τ_{h}	2.57(8)	hrs
T_2 heating	$T_{\max}$	78.0(6)	°C
T_2 heating	τ_{h}	2.58(7)	hrs
T_3 heating	$T_{\max}$	107(11)	°C
T_3 heating	τ_{h}	0.82(11)	hrs
$T_1/T_2/T_3$ cooling	$T_{\min}$	25.2	°C
T_1 cooling	$T_{0,\mathrm{c}}$	79.2(7)	°C
T_1 cooling	τ_{c}	2.83(8)	hrs
T_2 cooling	$T_{0,\mathrm{c}}$	77.4(7)	°C
T_2 cooling	τ_{c}	2.86(9)	hrs
T_3 cooling	$T_{0,\mathrm{c}}$	89(10)	°C
T_3 cooling	τ_{c}	1.83(46)	hrs
p cooling	$p_{\min}$	$4.3(7)\ 10^{-7}$	mbar
p cooling	p_1	$2.3(3)\ 10^{-6}$	mbar
p cooling	τ_{pc1}	3.2(6)	hrs
p cooling	p_2	$2.5(4)\ 10^{-6}$	mbar
p cooling	τ_{pc2}	0.5(1)	hrs

2.3.2. Cryo Pump

It is well known that gases condensate on cold surfaces. This effect is used to build cryo pumps, by placing a surface inside the vacuum chamber and cooling it below 120 K [22]. Atoms and molecules are not pumped out of the system, but still can be bound to this surface during measuring cycles.
The measurement chamber has already been supplied with such a cryo pump and so it was obvious that a further reduction of water molecules during the measurements can be achieved by adding an additional pump to the pickup chamber. It was decided to run the pump with liquid nitrogen and to place the reservoir inside the chamber because of the better isolation in absence of convection. Further on, it should be possible in the future to implement a QMS in the pickup chamber, meaning that there had to be a block-out in the trap, where the rod system can protrude.
Taking all these points into account led to the final design of the cryo pump, consisting of two closed cylinders which are filled with the coolant and whose barrels are the adsorbing surfaces at the same time. The cylinders are connected by a small connection tube and

mounted on the upper chamber wall with two flanges, which are in turn connected to the reservoir with two additional small tubes. Because of the low temperature it is not possible to take conventional O-rings for sealing and so homemade sealings of PTFE are used. All other parts are manufactured of stainless steel. Drawings of the pump can be found in Sec. C.1. Sec. A.1.2 contains an estimation for the operation time with one filling of liquid N_2.
There is a noticeable reduction of water in the pickup chamber, which can be seen by monitoring the pressure (see Tab. 2.4) or by comparing QMS measurements. However, there is still room for technical improvements. As mentioned above and evident in the drawings (Sec. C.1), the reservoir is hanging on two tubes. Those tubes stick out of the upper vacuum chamber wall and are used to fill the reservoir. While the liquid nitrogen is filled in one tube, steam of evaporated N_2 should stream out of the other. However, the inner diameter of the tubes is 3 mm which turned out to be too small. For fast filling, it is therefore necessary to pump the steam out of the reservoir through the second tube, e.g. by using a vacuum cleaner. This problem could be overcome by a redesign, using tubes with a larger diameter.
Also the second problem concerns the two filling tubes. During operation of the pump, water condensates on the outsticking tubes and runs along the outer surfaces to the flanges. There it crystallizes, which can lead to leaks as result of volume enlargement. It would be possible to prevent this effect by installing a shell consisting of a second tube around the existing ones (see Fig. 2.5). If there is only a small thermal contact between the tubes, the outer one would still be at room temperature and no condensation could take place.

The obtainable final pressures after the adaptation of the vacuum system are listed in Tab. 2.4.

Table 2.4.: Final pressures p in the separated vacuum chambers after adaptation of the vacuum system. Subscripted indices stand for: sc...source chamber, pc...pickup chamber, mc...measurement chamber, QMS...section of quadrupole mass spectrometer.

	$p_{\mathrm{sc}}/10^{-5}\,\mathrm{mbar}$	$p_{\mathrm{pc}}/10^{-8}\,\mathrm{mbar}$	$p_{\mathrm{mc}}/10^{-7}\,\mathrm{mbar}$	$p_{\mathrm{QMS}}/10^{-8}\,\mathrm{mbar}$
without cryo pump	2.8	12.0	2.2	1.9
with cryo pump	—	9.0	2.0	—

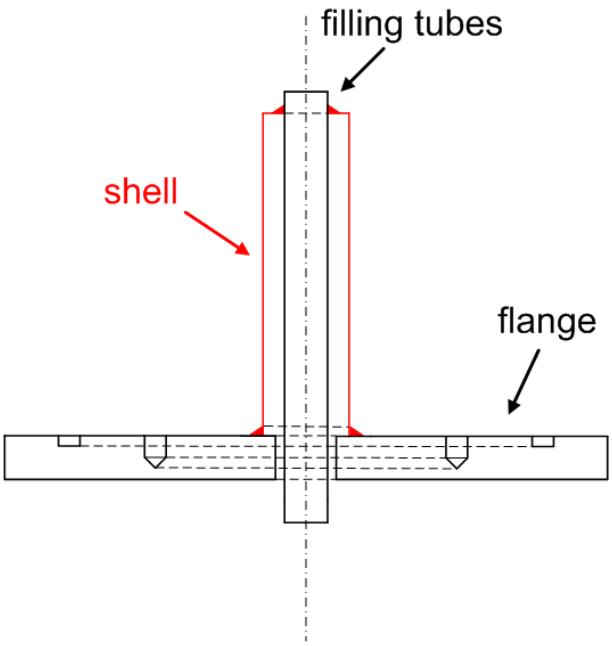

Figure 2.5.: Possible thermal insulation of cryo pump filling tubes. The additional part is drawn in red. Note that this is only a schematic depiction and not to scale. A detailed drawing of the flange can be found in Sec. C.1.

2.3.3. Additional Improvements of the Vacuum System

Molecular Sieve Foreline Trap

The foreline vacuum system of the pickup chamber and the measurement chamber is pumped by a rotary vane pump (Varian, CD700). Back streaming oil of this pump contaminated the foreline vacuum tubes in the past. In order to stop this process, a molecular sieve foreline trap (Kurt J. Lesker, inline straight style) has been mounted right after the rotary vane pump. Further on, the contaminated foreline vacuum tubes have been exchanged for clean ones. The changes led to a reduction of pump oil inside the vacuum chambers, which can be seen in QMS measurements.
To maintain the proper functioning of the trap, it is necessary to regenerate the sieve in certain time intervalls. Therefore one disconnects the foreline tubes after the trap, so that the trap is still pumped by the rotary vane pump and then turns on the integrated heater. Monitoring of the regeneration process is possible by attaching a fore-vacuum gauge head instead of a blind flange. In a first test, the pressure measured after the trap decreased from $4 \cdot 10^{-4}$ mbar to $1.6 \cdot 10^{-4}$ mbar after 7 hours of regeneration.
It is important to note that also other gases like e.g. water vapour are pumped by the foreline trap and then set free in the regeneration process. To avoid dilution of the pump oil it is therefore necessary to open the gas ballast of the rotary vane pump while heating the trap.

Nitrogen Gas Ventilation

Sometimes it is necessary to vent a vacuum chamber only for a very short time to adjust the experimental setup. However, if ambient air streams into the chamber, unwanted particles or molecules like e.g. H_2O can adsorb on the chamber wall. Their removal by pumping the system takes a long time, even if assisted by a bake out process (see Sec. 2.3.1).
It is possible to minimize contamination by venting the system with gaseous nitrogen instead of ambient air. For this purpose, the venting valves of the turbo pumps were connected to a high pressure nitrogen gas line. After the ventilation a constant nitrogen flow out of the chamber prevents air intrusion. To avoid damage of the respective vacuum chamber caused by overpressure, it is very important to loosen the screws of at least one flange before opening the ventilation valve.

3. Results

3.1. ^{87}Rb Electron Spin Resonance on Helium Nanodroplets: The Influence of Optical Pumping

The following is an excerpt from a publication by Alexander Volk, Johannes Poms, Markus Koch, and Wolfgang E. Ernst, that was accepted as part of the "J. Peter Toennies Festschrift" in *The Journal of Physical Chemistry A*, and will appear soon [50] [1]. In accordance with the rest of this work, only the evaluation of the hyperfine coupling constant a_{HFS} and the related measurement results are reported. The presentation and modelling of the influence of optical pumping on the optained signals is part of the master thesis of Johannes Poms, which will appear soon [41].

3.1.1. Abstract

Hyperfine resolved electron spin resonance (ESR) measurements of single rubidium (^{87}Rb) atoms isolated on superfluid helium nanodroplets are presented. In accordance with our previous work on ^{85}Rb, we find a relative increase of the hyperfine constant a_{HFS} by about 400 ppm, depending on the size of the droplets. In order to optimize the ESR signal intensities, the processes of optical pumping of Rb atoms on helium droplets and of optical detection of the ESR transitions are investigated in detail. Both the laser intensity and polarization influences the ESR signal intensities. A simple model for optical pumping of Rb atoms on helium droplets is presented, which agrees well with the experimental results.

3.1.2. Introduction

The marriage of magnetic resonance spectroscopy and helium nanodroplet isolation spectroscopy has recently been achieved. Hyperfine resolved electron spin resonance (ESR) spectra of single alkali-metal atoms (^{39}K and ^{85}Rb) located on the surface of superfluid helium nanodroplets ($\mathrm{He_N}$) have been presented [28, 30]. The ESR spectra consist of extremely sharp lines, and the ESR peaks of alkali-metal atoms located on $\mathrm{He_N}$ (the

[1] At present only the online puplication is available at http://dx.doi.org/10.1021/jp112385d

on-droplet peaks) are shifted by a few hundred parts per million (ppm) with respect to those of the bare atoms (the free-atom peaks). These shifts exhibit the influence of the He environment on the alkali-metal valence electron, result from an increase of the electron spin density at the alkali-metal nucleus, and can be modeled as a raise of the hyperfine constant a_{HFS}: $\delta a_{\mathrm{HFS}}/a_{\mathrm{HFS}} \sim 400\,\mathrm{ppm}$ for Rb and $\delta a_{\mathrm{HFS}}/a_{\mathrm{HFS}} \sim 300\,\mathrm{ppm}$ for K ($\delta a_{\mathrm{HFS}} = a_{\mathrm{HFS,\,droplet}} - a_{\mathrm{HFS,\,free}}$) [28]. The Landé factor g_{J} remains unchanged within the experimental uncertainties of a few ppm. δa_{HFS} turned out to depend on the droplet size and the system ^{85}Rb–He$_{\mathrm{N}}$ could be well characterized [29]. For the mean number of droplet sizes in the range of $\bar{N} \approx 1000$ to ≈ 15000, a change of $\delta a_{\mathrm{HFS}}/a_{\mathrm{HFS}}$ of about 10% from $\sim 390\,\mathrm{ppm}$ to $\sim 430\,\mathrm{ppm}$ could be observed. The results are supported by a simple model, where the effect is semiempirically estimated based on computed He densities and electron wave functions. Furthermore, the observation of about 50 Rabi oscillations demonstrates that the alkali-metal–He$_{\mathrm{N}}$ system exhibits minimal dephasing [28].
The high-resolution of the ESR spectra and their sensitivity to the droplet size motivated us to use surface-located alkali-metal atoms as spin labels for ESR silent species, which are located inside the He$_{\mathrm{N}}$. We expect additional line shifts to occur as a consequence of the direct van der Waals interaction between the alkali-metal atom and species with a high polarizability and/or a permanent electric dipole moment. Line splittings may be observed if species with nuclear spins are present. Shorter dephasing times will be directly observable as a reduced number of Rabi oscillations. The value of all mentioned influences can be tuned via the droplet size, which is a convenient handle to control the distance between the probe and the complex. For this generalization of the method toward ESR silent species it is very important to use alkali-metal atoms with strong hyperfine interaction, e.g. ^{87}Rb with $a_{\mathrm{HFS}} = 3417\,\mathrm{MHz}$ or ^{133}Cs with $a_{\mathrm{HFS}} = 2298\,\mathrm{MHz}$ (^{85}Rb: $a_{\mathrm{HFS}} = 1012\,\mathrm{MHz}$) [3]. These elements exhibit higher absolute line shifts and should provide better sensitivity for additional influences.
In this work we present detailed measurements on the ^{87}Rb–He$_{\mathrm{N}}$ system. First, a complete ESR spectrum is presented. Then, to investigate the droplet size dependence, the shift of one particular ESR line is shown for different $\bar{N}$, before the dependence of δa_{HFS} (obtained from full ESR scans, also at different $\bar{N}$) is depicted. Finally, optical pumping of single ^{87}Rb atoms on He$_{\mathrm{N}}$ is investigated. To determine the influence of the pumping conditions, two measurements were carried out: first, the amplitudes of all ESR transitions were recorded with the laser beams in σ^+ and in σ^- polarization. Second, the dependence of the highest-field ESR transition amplitude on the laser power was monitored for σ^+ and for σ^- polarization. A simple model for pumping of Rb atoms on He$_{\mathrm{N}}$, which is presented at the end, is found to agree well with the experimental results.

3.1.3. Experimental Section

A detailed description of the experimental setup and the scheme of ESR on He_N has been published elsewhere [30]. In brief, He_N are produced via supersonic expansion of He gas through a cold nozzle into vacuum (nozzle diameter 5 μm, nozzle temperature $T_0 = 12.5$–23 K, stagnation pressure $P_0 = 50$ bar, mean number droplet size $\bar{N} \approx 1000$–15000 He atoms). All droplet sizes $\bar{N}$ stated here are assigned using data from the literature [20] (Since no droplet sizes are reported for the nozzle pressure we used (50 bar), the closest available data were taken (40 bar)). After doping with, on average, one Rb atom (natural abundances: ^{85}Rb: 72.2%, ^{87}Rb: 27.8% [35]) per droplet, the doped droplets enter the homogeneous magnetic field region (B_0) of an electromagnet. The spin-population relaxation time T_1 on He_N is long (> 2 ms [5, 38]), so that a pump laser beam is used to create a net electron spin polarization by means of optical pumping [18]. Optical pumping is based on different excitation probabilities of individual hyperfine ground-states. Usually single frequency lasers are used [15], but on He_N a significant broadening of electronic transitions due to a perturbation by the droplet [8, 30] prevents this mechanism. Therefore, a magnetic circular dichroism (MCD) scheme is used, which applies a circularly polarized pump laser beam to selectively address magnetic substates. The low optical density of the He_N beam prevents direct detection of ESR transitions and optically detected magnetic resonance (ODMR) is the key that makes the detection of ESR on He_N possible. A microwave (MW) cavity, with entrance and exit holes for the droplet beam, is located between the pump and the probe laser beam (both laser beams have the same helicity). The MW frequency (ν_0) is kept fixed while B_0 is scanned and ESR transitions are detected indirectly as an increase of the laser-induced fluorescence (LIF) signal, which is collected at the intersection of the probe laser beam with the droplet beam. Both laser beams are obtained from the same Ti:Al_2O_3 laser, which is tuned to the wavelength with the most efficient spin polarization and spin probe action on the droplet (detuned by $\sim 20\,\mathrm{cm}^{-1}$ to the blue from the free atom $D1$ transition) [30].

To determine the value of B_0 with highest possible accuracy, a reference ESR signal from gas phase Rb atoms (which are effusing from the pickup cell) is generated with a second laser. We use a grating stabilized single-mode diode laser, which is tuned to the gas phase $D1$ line of Rb atoms and split and polarized in the same way as the Ti:Al_2O_3 laser. Because of the use of both lasers, a magnetic field scan results in two separated ESR peaks, the free-atom peak and the on-droplet peak.

All peaks are fitted with Gaussian functions. The actual free-atom ESR positions are calculated for the MW frequency in use with the Breit–Rabi formula [31], taking the known values of the hyperfine constant a_{HFS}, the Landé factor g_{J}, and the nuclear factor g_{I} [3]. The on-droplet line positions are obtained by adding the measured line shifts to the free-atom positions. All on-droplet positions are then fitted with the Breit–Rabi formula again, but this time a_{HFS} and g_{J} are allowed to differ by δa_{HFS} and δg_{J} from the free-atom

values.
With one unpaired electron, ^{87}Rb has an electron spin quantum number (QN) of $S = 1/2$ and two possible projections $m_S = \pm 1/2$ along the quantization axis given by B_0. For electronic excitations only $D1$ ($5^2P_{1/2} \leftrightarrow 5^2S_{1/2}$) transitions are considered for this work, with a total angular momentum QN $J = 1/2$ in both the ground and the excited state. ^{87}Rb has a nuclear spin QN of $I = 3/2$ and the four possible projections are $m_I = \pm 3/2$, and $\pm 1/2$. The four ESR transitions are given by the selection rules $\Delta m_I = 0$ and $\Delta m_J = \pm 1$. The electronic ground state ($5^2S_{1/2}$) and the first electronically excited state ($5^2P_{1/2}$) are both split by the hyperfine interaction with a total angular momentum QN including the nuclear spin of $F = 1$ and $F = 2$.

3.1.4. Results

ESR line shifts induced by the He_N

Figure 3.1 shows a complete ESR spectrum of ^{87}Rb atoms on He_N. In the top panel the line positions of bare atoms are indicated, as obtained with the Breit–Rabi formula for a MW frequency of $\nu_0 = 9.44230\,\mathrm{GHz}$. The lower panel shows the line shifts induced by the He_N. Detailed B_0 scans across the four ESR lines consist each of the free-atom and the on-droplet peak; the free-atom peaks are located per definition at zero shift. The exact positions of the free-atom transition is given next to each scan. Values for the line shifts of each individual ESR transition are obtained from the separation of two Gaussian fits. These shifts are (from the lowest-field to the highest-field transition) $\Delta B_0 = -116(1)$, $-126(1)$, $-70(2)$, $+56(1)\,\mu\mathrm{T}$ (experimental error given in parentheses). Note that the $m_I = +3/2$ hyperfine line (red) exhibits a smaller shift than the one with $m_I = +1/2$ (blue). This is in contrast to ^{85}Rb[28], and can be explained with the larger hyperfine constant a_{HFS} of ^{87}Rb ($a_{HFS,87} \approx 3 \cdot a_{HFS,85}$). For the same MW frequency ^{87}Rb hyperfine lines lie in the transition region from the Zeeman regime to the Paschen–Back regime, where a decoupling of the nuclear spin and the electron spin takes place. In this region neither $|F\ m_F\rangle$ nor $|m_J\ m_I\rangle$ is a rigorously good basis set and the energy levels are curved (whereas they increase linearly with B_0 in the Zeeman and in the Paschen–Back regime). Also, the intensity of the individual on-droplet ESR peaks differs much more than was the case for ^{85}Rb[28]. This prompted us to investigate the influence of the pumping conditions on the ESR signal strength (see further down).

Droplet size dependence

In order to determine the droplet size dependence of the change of the hyperfine constant δa_{HFS}, ESR spectra at different nozzle temperatures were recorded. Figure 3.2 shows the lowest-field on-droplet ESR transition for different droplet sizes. The free-atom peak occurs at $B_0 = 0.1135950\,\mathrm{T}$ ($\nu_0 = 9.44230\,\mathrm{GHz}$). Five different droplet sizes, ranging from

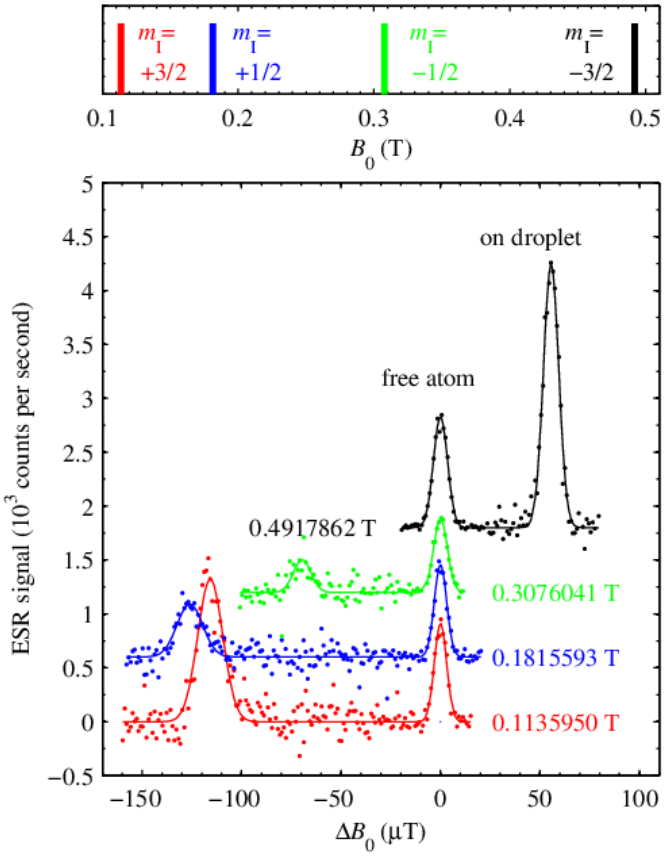

Figure 3.1.: ESR spectrum of ^{87}Rb on He_N. Top: Stick spectrum of the four ESR transitions $\Delta m_J = \pm 1$, $\Delta m_I = 0$ ($m_I = +3/2, +1/2, -1/2, -3/2$, from left to right) in free ^{87}Rb atoms. Bottom: Shift of the on-droplet ESR lines with respect to the free-atom lines, induced by the He_N (same colors as top panel, the traces are vertically offset by 600 counts per second each; all scans are averages of at least two separate measurements). The mean droplet size of $\bar{N} \approx 6000$ is obtained with $T_0 = 17\,\mathrm{K}$. The free-atom lines appear by definition at zero shift and the corresponding value of B_0 is indicated beside for $\nu_0 = 9.44230\,\mathrm{GHz}$. Each trace is fitted (solid lines) with two Gaussian functions.

$\bar{N} \approx 1000$ to $\bar{N} \approx 15000$ He atoms per droplet, are obtained with $T_0 = 23$, 20, 17, 14, and 12.5 K. The individual line shifts are (from smaller to larger droplets): $\Delta B_0 = -109(3)$, $-113(1)$, $-116(1)$, $-119(1)$, $-125(1)\,\mu$T. The observed shifts of the lowest-field ESR transition of ^{87}Rb are larger by a factor of 2.6 than those of ^{85}Rb [29]. Figure 3.3 shows the droplet size dependence of a_{HFS} for ^{87}Rb (circles), together with values for ^{85}Rb (squares) from Ref. [29]. Droplet sizes were obtained with corresponding nozzle temperatures T_0, given at the top axis. For $T_0 = 14$, 17, and 20 K full ESR spectra were used to determine

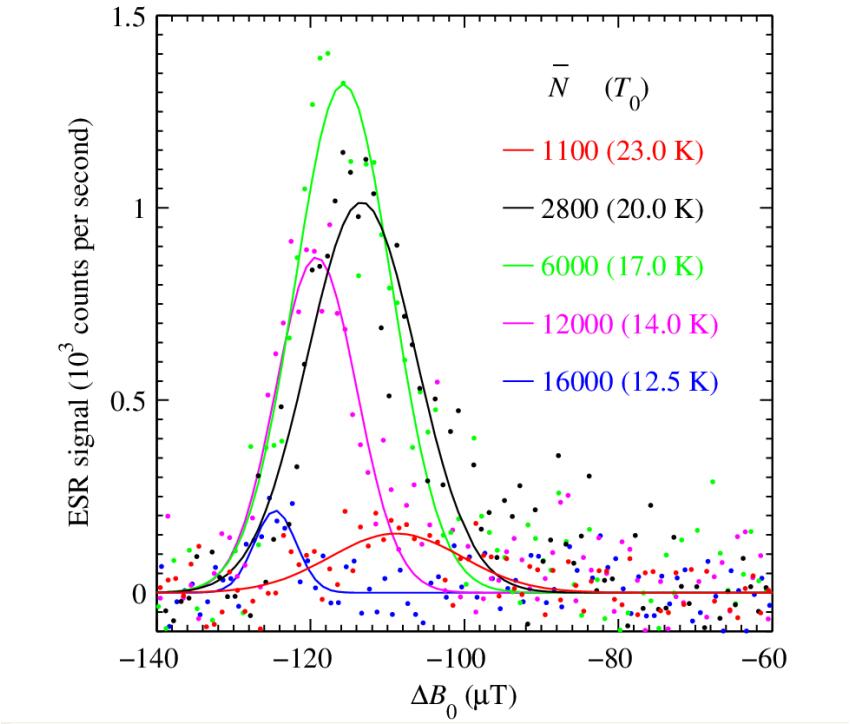

Figure 3.2.: Droplet size dependence of the lowest-field on-droplet ESR transition ($I = 3/2$, $m_I = +3/2$). Droplet sizes $\bar{N}$ and the corresponding nozzle temperatures T_0 (in brackets) are given in the legend. The data points are fitted with Gaussian functions.

$\delta a_{\mathrm{HFS}}/a_{\mathrm{HFS}}$, while for $T_0 = 12.5$, and 23 K only the lowest-field and the highest-field ESR transitions could be included, since the two middle transitions were too weak to be fitted (at the corresponding source conditions ESR signals appear to be very weak, cf. 3.1 and 3.2). The weak ESR signal is also the reason for the large uncertainty of the data point at $T_0 = 12.5$ K.

Influence of pumping conditions

Figure 3.4 shows the measured ^{87}Rb on-droplet ESR peak amplitudes (full triangles) of all four ESR transitions (cf. Figure 3.1) with different helicity of the laser beams. Both the pump and and probe laser beam were used in σ^+ (upward-pointing triangles) and in σ^- (downward-pointing) polarization. In order to simulate this behavior, a simple pump model (open triangles, see next section) was used, also for σ^+ (upward-pointing) and for σ^- (downward-pointing) polarization.

In Figure 3.5 the dependence of the highest-field ESR transition amplitude on the laser power is depicted for σ^+ (upward-pointing triangles) and for σ^- (downward-pointing triangles) polarization of the laser beams. Both the pump and the probe laser beam have been simultaneously reduced in power, while the ratio of the two powers was kept con-

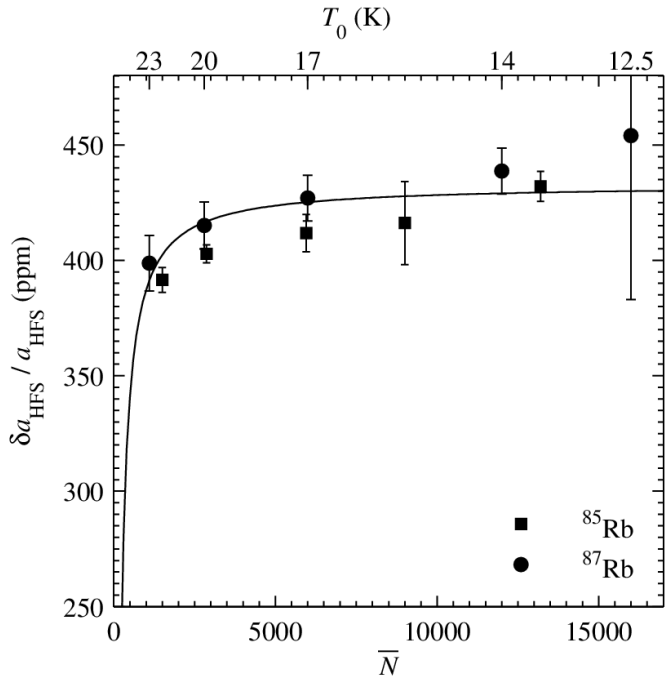

Figure 3.3.: Droplet size dependence of the relative change of the hyperfine constant $\delta a_{\mathrm{HFS}}/a_{\mathrm{HFS}}$ for ^{87}Rb atoms on He_N (circles). Results for ^{85}Rb–He_N (squares) are also shown [29]. The corresponding nozzle temperatures are reported on the top axis. The solid line represents a $1/N$ trend which serves as a guide to the eye.

stant: $P_{\mathrm{pump}}/P_{\mathrm{probe}} \approx 9$. Results of the simulation are shown for σ^+ (continuous line) and for σ^- (dashed line) polarization (see next section).

The discrepancies between the measured and simulated ESR peak amplitudes in Figure 3.4 and Figure 3.5 may be due to the following facts: (1) The perturbation by the He_N affects the selection rules for electronic dipole transitions of the Rb atoms [30]. This influences the pumping and probing mechanism. (2) The MW power was adjusted at the lowest-field ESR transition in order to obtain a maximum signal amplitude, and then kept constant for the other ESR transitions. The Rabi-oscillation pattern, however, depends on the magnetic dipole transition matrix element, which in turn might be slightly different for the four ESR transitions because of an alteration of the wavefunction due to the decoupling of the electron spin and the nuclear spin. Such a change of the Rabi-oscillation pattern results in a decrease of the measured ESR peak amplitude.

Optical pumping of Rb Atoms on He_N

In order to understand the differences in ESR signals of different lines and laser polarizations (see Fig. 3.4), a simple model on optical pumping of alkali-metals on He_N has been

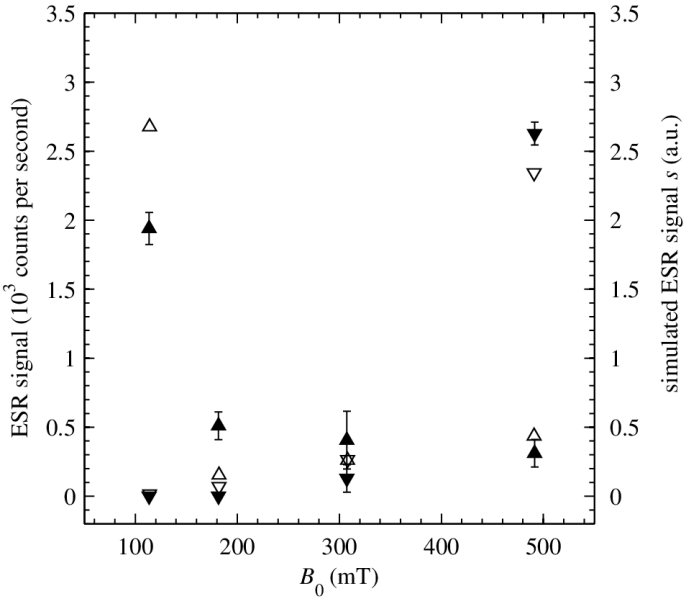

Figure 3.4.: Measured amplitudes of the ESR lines (full triangles) as obtained with σ^+ (upward-pointing) and with σ^- (downward-pointing) laser polarization, plotted at the magnetic field B_0 where they appear for $\nu_0 = 9.442\,\mathrm{GHz}$. The power of the pump laser beam was $P_{\mathrm{pump}} = 2.8\,\mathrm{W}$, and that of the probe laser beam was $P_{\mathrm{probe}} = 320\,\mathrm{mW}$. The simulated values s of the ESR signal (open triangles) for σ^+ (upward-pointing) and for σ^- (downward-pointing) polarization are obtained with $N = 72$ iteration steps simulating the interaction with the pump laser beam and $M = 18$ iteration steps simulating the interaction with the probe laser beam.

indroduced. As this part is the subject of the work of Johannes Poms (see Ref. [41]), the model is not described in detail here.
In brief, the change in the population of the ground state hyperfine levels during one excitation–re-emission cycle (i.e. one pumping cycle induced by the pump laser) can be obtained by calculating the electronic dipole transition matrix elements for one excitation and a subsequent spontaneous emission. In strong magnetic fields (which can be seen as perturbations of the Hamiltonian) one has to take into account further, that the substates are a linear combination of unperturbed states (see Sec. 1.3.2). The result is a propability vector, which changes with each pumping cycle.
ESR transitions are simulated by exchanging the corresponding population probabilities of the two involved hyperfine levels. To get the intensity of the LIF signal, a certain number of further excitation–re-emission cycles is simulated for the probe laser beam, now using the population distribution obtained from the former simulation after the ESR transition.

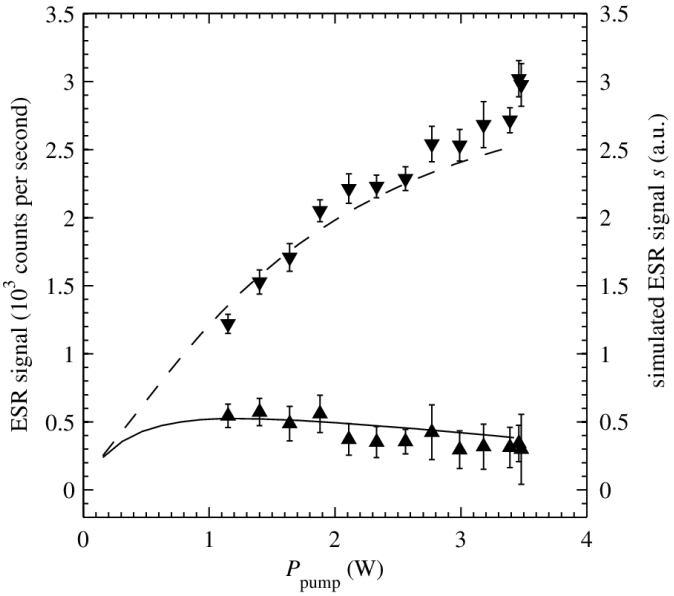

Figure 3.5.: Dependence of the highest-field ESR transition amplitude on the power of the pump laser beam P_{pump} for σ^+ (upward-pointing triangles) and for σ^- (downward-pointing triangles) polarization of the laser beams. The simulated curves for σ^+ (continuous line) and for σ^- (dashed line) polarization are obtained by increasing N and M (see next section) in integer steps from zero to $N = 88$ and $M = 22$, and keeping their ratio constant at $N/M = 4$. For $P_{\text{pump}} = 2.8\,\text{W}$, we used $N = 72$ and $M = 18$ (cf. Figure 3.4).

3.2. Evaluation of δa_{HFS} for single ESR-lines

3.2.1. Motivation

As described in Sec. 3.1, δa_{HFS} and δg_{J} are determined by first fitting all ESR peaks with Gaussian functions, calculating the positions of the on-droplet peaks with the help of the free atom peaks and subsequently fitting the on-droplet peaks with the Breit–Rabi formula by variation of the parameters a_{HFS} and g_{J}. All necessary Matlab programs can be found on the enclosed CD (see Sec. B.1).
In the past, full sets of six (^{85}Rb) or four (^{87}Rb) ESR-lines were used to determine δa_{HFS} and δg_{J}, which is in fact an overparameterisation of the system of equations. While this method leads to improved fit accuracy for precise measurements and Gauss-fits, the results can also be distorted by deviations of a single line.
Fig. 3.6 and 3.7 show the on-droplet ESR lines of ^{85}Rb and ^{87}Rb respectively. One can see that not for all transitions the data points can be perfectly represented by a symmetric Gaussian function. Instead, the asymmetry of the data points leads to a small offset between their maxima and those of the Gaussian functions. This is especially the case for the ^{87}Rb on-droplet transition at 113.63 mT (see Fig. 3.7), because here the droplet size distribution (see Sec. 1.1.1) plays a significant role.
Note that the low signal to noise ratios for the two transitions at intermediate magnetic field strengths in Fig. 3.7, are a result of the low ESR signals as depicted in Fig. 3.4. The reason for these low signals is due to the optical pumping process as will be explained in the work of Johannes Poms [41].
For spin labeling experiments, the interactions between ESR silent species and the spin label may only lead to small changes of the line shapes, positions, or intensities. It will therefore be important to take these asymmetries, which are mainly a result of the fact that not all $\mathrm{He_N}$ droplets have the same size but follow a log-normal distribution (see Eqn. 1.2), into account when simulating the line shapes. For these simulations, which are the subject of current work, it is desirable to evaluate δa_{HFS} and δg_{J} for every single ESR line in order to avoid the averaging as explained above.
Scanning a line with large shift and a good signal to noise ratio (e.g. the one at 113.63 mT in Fig. 3.7) at source conditions where the droplet size distribution has already been measured (see Refs. [20, 33]), can be used to evaluate the relation between δa_{HFS} and the droplet size $\bar{N}$ as done in Fig. 3.3, but for this single ESR line. It is then possible to measure the line shape at different source conditions, where the asymmetry changes due to a different droplet size distribution, and to evaluate the new droplet size distribution by simulating the line shape.

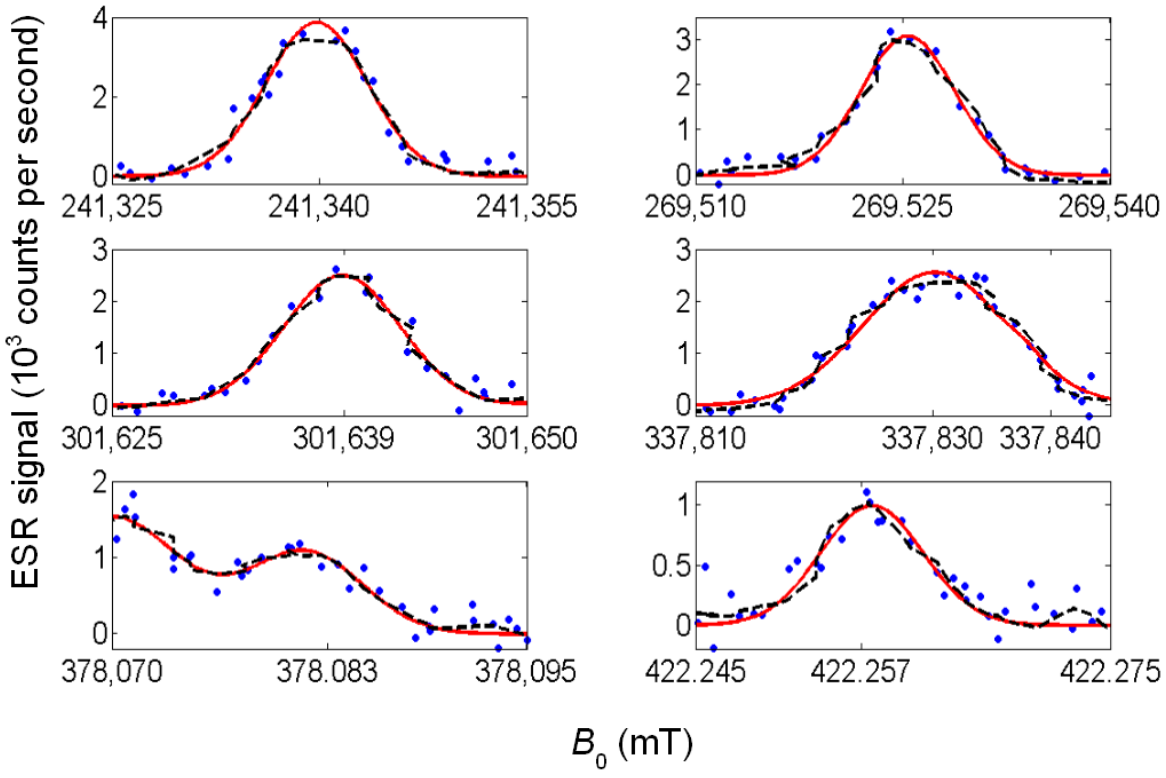

Figure 3.6.: The six on-droplet ESR lines of ^{85}Rb, corresponding to datasets 70-75 of Tab. 3.2 and B.1. The measured data points (blue dots) are fitted with a Gaussian function (solid red). Also indicated is a smoothing of the data points (dashed black) using the Matlab function *smooth*, with the algorithm *sgoly(span,order)*. The span for the moving average was set to 25, the order of the used polynomial was taken to be 5. Note that at $B_0 = 337.830\,\mathrm{mT}$ the on-droplet peak and the free-atom peak are very close to each other and can not be resolved. To overcome this problem, the two peaks are scanned seperately, i.e. only the Ti-Saph or the Diode laser is used during one scan. At $B_0 = 378.070\,\mathrm{mT}$ there is still an overlap, with the free-atom peak being at lower field strengths.

3.2.2. Method

The evaluation of full sets of ESR lines (i.e. four lines for ^{87}Rb and six for ^{85}Rb) of ESR transitions using a_{HFS} and g_{J} as free paramters, leads to only small changes of the latter in most cases (see Tab. 3.2 and B.1). In addition, the relative uncertainties of δg_{J} are large. This suggests a new analysis method, where a_{HFS} is the only variable parameter in the Breit–Rabi equation and δg_{J} is set to zero. Using the same Matlab programs as

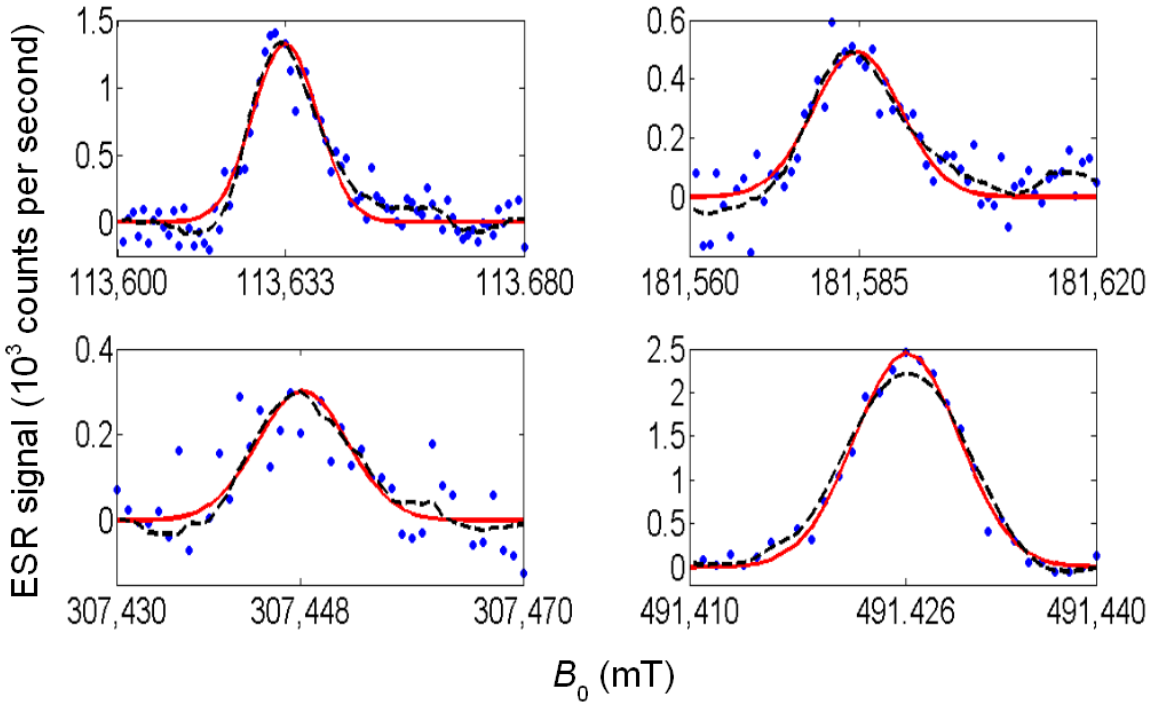

Figure 3.7.: The four on-droplet ESR lines of ^{87}Rb, corresponding to datasets 76-79 of Tab. 3.2 and B.1. The measured data points (blue dots) are fitted with a Gaussian function (solid red). Also indicated is a smoothing of the data points (dashed black) using the Matlab function *smooth*, with the algorithm *sgoly(span,order)*. The span for the moving average was set to 25, the order of the used polynomial was taken to be 5. One can see an asymmetry of the peaks, especially for the two lines at lower magnetic fields.

before with a fixed value of g_J, but passing values from 0 to 1000 ppm for δa_{HFS}, leads to the calculated magnetic field shifts depicted in Fig. 3.8. The MW-frequency was held constant at 9442 MHz.

Although unapparent from Eqn. 1.23-1.25, there is a linear relationship between the ESR peak shifts and a change of the hyperfine coupling constant in the investigated regime. This could also be confirmed by fitting a third order polynomial through the calculated data points, where the linear terms turned out to be 8 orders of magnitude higher than quadratic or cubic terms. Further on, the same calculations were done assuming MW-

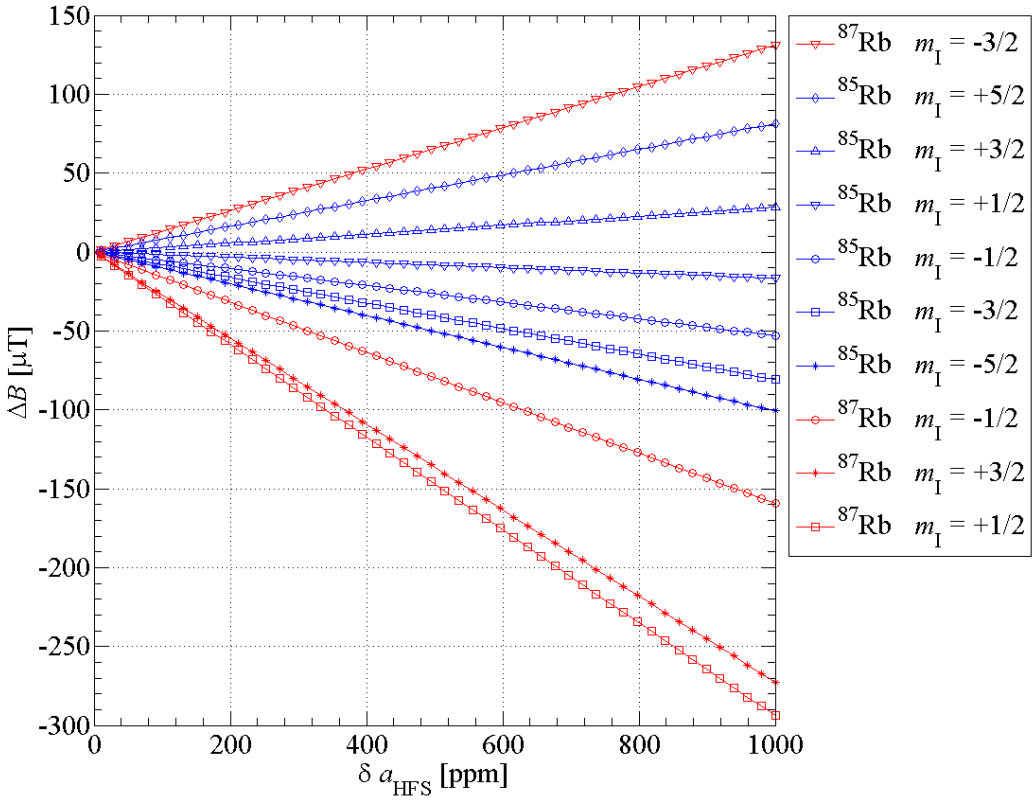

Figure 3.8.: Hyperfine constant dependence of ESR signal shifts for constant g_J. The shift ΔB of the on-droplet ESR peaks in respect to the free-particle lines (see Fig. 3.1) was calculated using the Breit–Rabi formula (Eqn. 1.23-1.25) for different values of δa_{HFS}. The results are depicted for ^{85}Rb (blue) and ^{87}Rb (red). Different ESR transitions $\Delta m_J = \pm 1$, $\Delta m_I = 0$ are labeled with m_I.

frequencies of 9441 MHz and 9443 MHz, to take into account small variations, which are necessary to compensate thermal induced size variations of the MW-cavity. The slopes of the straight lines changed less than 0.3 %, so that it can be justified to use a constant value.
All these considerations above lead to a set of linear equations, with which it is possible to evaluate δa_{HFS} by using the measured magnetic field shift ΔB of one ESR line:

$$\delta a_{\mathrm{HFS_i}} = \frac{\Delta B}{k_{\mathrm{i}}} \tag{3.1}$$

The index i accounts for the fact, that different ESR transition lines have different slopes k_{i} for the straight lines (see Fig. 3.8). i therefore contains the information which isotope

has been used and for which transition line the calculation is performed, e.g. $i = 87, -3/2$ for the topmost straight line in Fig. 3.8. The respective slopes are listed in Tab. 3.1.

Table 3.1.: Straight line slope values k (see Fig. 3.8) according to Eqn. 3.1 for different isotopes and transitions.

k / $\frac{\mu\mathrm{T}}{\mathrm{ppm}}$	isotope	m_I
+0.0813	^{85}Rb	+5/2
+0.0284	^{85}Rb	+3/2
-0.0166	^{85}Rb	+1/2
-0.0530	^{85}Rb	-1/2
-0.0809	^{85}Rb	-3/2
-0.1008	^{85}Rb	-5/2
-0.2727	^{87}Rb	+3/2
-0.2937	^{87}Rb	+1/2
-0.1592	^{87}Rb	-1/2
+0.1311	^{87}Rb	-3/2

Note that the slopes for ^{87}Rb do not increase linearly with m_I, reflecting the transition from the Zeeman regime to the Paschen–Back regime as mentioned for the measured line shifts in Sec. 3.1.4.

3.2.3. Results

Tab. 3.2 contains the results for both the change of a_HFS as calculated for full sets and as calculated for individual ESR lines (δa_HFS). More detailed information regarding the measurement conditions, like measurement type, source conditions and date of measurement, can be found in Tab. B.1.
Note that $\overline{\delta a_\mathrm{HFS}}$ and $\overline{\delta g_\mathrm{J}}$ have the same values for all datasets that belong to the respective full set of ESR transitions, e.g. datasets 25, 30, 35, 40, 45 and 50 were used to fit one value of a_HFS. On the other hand, for datasets of individual ESR lines (no full set) the values of $\overline{\delta a_\mathrm{HFS}}$ and $\overline{\delta g_\mathrm{J}}$ can not be evaluated (e.g. dataset 7).

Table 3.2.: Values for δa_{HFS} calculated for single ESR lines. The column *dataset* is aequivalent to the one in Tab. B.1. $\overline{\delta a_{\mathrm{HFS}}}$ and $\overline{\delta g_{\mathrm{J}}}$ are calculated by variation of a_{HFS} and g_{J}, using a full set of ESR lines (values partially taken from Ref. [27]) B_0 is the magnetic field where the ESR transition occurs for the free atoms, while ΔB is the shift of the droplet peaks in respect to B_0. T_0 is the source temperature.

dataset	isotope	B_0 / mT	T_0 / K	ΔB / μT	$\overline{\delta a_{\mathrm{HFS}}}$ / ppm	$\overline{\delta g_{\mathrm{J}}}$ / ppm	δa_{HFS} / ppm
54	^{87}Rb	113.6	23	-109.1(23)	399(12)	–	400(8)
55	^{87}Rb	113.6	20	-113.2(8)	414(5)	1(3)	415(3)
56	^{87}Rb	113.6	17	-115.7(5)	427(10)	1(7)	424(2)
76	^{87}Rb	113.6	17	-116.5(5)	430(9)	1(6)	427(2)
57	^{87}Rb	113.6	14	-119.2(7)	437(7)	1(5)	437(3)
58	^{87}Rb	113.6	12.5	-124.7(13)	454(71)	–	457(5)
59	^{87}Rb	181.6	20	-121.3(20)	414(5)	1(3)	413(7)
60	^{87}Rb	181.6	17	-125.9(9)	427(10)	1(7)	429(3)
77	^{87}Rb	181.6	17	-127.3(20)	430(9)	1(6)	433(7)
61	^{87}Rb	181.6	14	-127.2(17)	437(7)	1(5)	433(6)
7	^{85}Rb	241.6	22	-41.4(3)	–	–	411(3)
18	^{85}Rb	241.6	22	-40.7(5)	393(13)	8(3)	404(5)
24	^{85}Rb	241.6	22	-40.8(9)	392(5)	6(1)	405(9)
8	^{85}Rb	241.6	20	-42.8(3)	–	–	425(3)
25	^{85}Rb	241.6	20	-42.0(3)	403(4)	5(1)	416(3)
9	^{85}Rb	241.6	18	-43.3(2)	–	–	430(2)
1	^{85}Rb	241.6	17	-43.1(2)	427(3)	0(1)	428(2)
26	^{85}Rb	241.6	17	-42.8(4)	412(8)	6(2)	425(4)
70	^{85}Rb	241.6	17	-43.6(53)	428(5)	2(1)	433(2)
10	^{85}Rb	241.6	16	-44.1(2)	–	–	438(2)
27	^{85}Rb	241.6	15	-43.4(3)	416(18)	7(4)	431(3)
11	^{85}Rb	241.6	14	-44.9(1)	–	–	446(1)
12	^{85}Rb	241.6	13	-45.9(3)	443(10)	7(2)	455(3)
28	^{85}Rb	241.6	13	-44.6(4)	432(7)	6(1)	443(4)
19	^{85}Rb	270.0	22	-33.7(4)	393(13)	8(3)	417(5)
29	^{85}Rb	270.0	22	-33.5(5)	392(5)	6(1)	415(6)
30	^{85}Rb	270.0	20	-34.1(3)	403(4)	5(1)	422(4)
2	^{85}Rb	270.0	17	-34.9(2)	427(3)	0(1)	431(2)
31	^{85}Rb	270.0	17	-34.8(2)	412(8)	6(2)	430(3)
71	^{85}Rb	270.0	17	-35.0(3)	428(5)	2(1)	433(3)
32	^{85}Rb	270.0	15	-35.4(2)	416(18)	7(4)	437(3)

dataset	isotope	B_0 / mT	T_0 / K	ΔB / μT	$\overline{\delta a_{\mathrm{HFS}}}$ / ppm	$\overline{\delta g_{\mathrm{J}}}$ / ppm	δa_{HFS} / ppm
13	^{85}Rb	270.0	13	-37.4(3)	443(10)	7(2)	463(4)
33	^{85}Rb	270.0	13	-36.4(4)	432(7)	6(1)	449(5)
20	^{85}Rb	301.8	22	-23.6(3)	393(13)	8(3)	446(6)
34	^{85}Rb	301.8	22	-22.8(3)	392(5)	6(1)	430(6)
35	^{85}Rb	301.8	20	-23.1(2)	403(4)	5(1)	436(4)
3	^{85}Rb	301.8	17	-22.8(1)	427(3)	0(1)	430(1)
36	^{85}Rb	301.8	17	-23.7(2)	412(8)	6(2)	447(3)
72	^{85}Rb	301.8	17	-23.4(3)	428(5)	2(1)	442(6)
37	^{85}Rb	301.8	15	-24.1(3)	416(18)	7(4)	455(7)
14	^{85}Rb	301.8	13	-26.3(4)	443(10)	7(2)	496(7)
38	^{85}Rb	301.8	13	-24.7(6)	432(7)	6(1)	467(11)
62	^{87}Rb	307.6	20	-67.8(80)	414(5)	1(3)	426(50)
63	^{87}Rb	307.6	17	-69.6(16)	427(10)	1(7)	437(10)
78	^{87}Rb	307.6	17	-69.8(17)	430(9)	1(6)	438(11)
64	^{87}Rb	307.6	14	-71.3(16)	437(7)	1(5)	448(10)
21	^{85}Rb	337.9	22	-9.5(2)	393(13)	8(3)	573(12)
39	^{85}Rb	337.9	22	-8.0(3)	392(5)	6(1)	481(17)
40	^{85}Rb	337.9	20	-8.1(2)	403(4)	5(1)	486(10)
4	^{85}Rb	337.9	17	-7.1(1)	427(3)	0(1)	430(4)
41	^{85}Rb	337.9	17	-8.9(2)	412(8)	6(2)	436(12)
73	^{85}Rb	337.9	17	-4.8(10)	428(5)	2(1)	291(60)
42	^{85}Rb	337.9	15	-8.6(3)	416(18)	7(4)	517(20)
15	^{85}Rb	337.9	13	-9.5(5)	443(10)	7(2)	572(33)
43	^{85}Rb	337.9	13	-9.4(4)	432(7)	6(1)	568(26)
22	^{85}Rb	378.1	22	6.4(3)	393(13)	8(3)	225(9)
44	^{85}Rb	378.1	22	8.0(3)	392(5)	6(1)	281(9)
45	^{85}Rb	378.1	20	8.9(2)	403(4)	5(1)	314(6)
5	^{85}Rb	378.1	17	12.0(1)	427(3)	0(1)	422(3)
46	^{85}Rb	378.1	17	8.5(2)	412(8)	6(2)	298(7)
74	^{85}Rb	378.1	17	10.9(5)	428(5)	2(1)	382(18)
47	^{85}Rb	378.1	15	8.4(1)	416(18)	7(4)	294(5)
16	^{85}Rb	378.1	13	9.3(2)	443(10)	7(2)	329(6)
48	^{85}Rb	378.1	13	9.5(4)	432(7)	6(1)	333(14)
23	^{85}Rb	422.2	22	29.6(2)	393(13)	8(3)	364(3)
49	^{85}Rb	422.2	22	29.5(3)	392(5)	6(1)	363(4)
50	^{85}Rb	422.2	20	30.5(2)	403(4)	5(1)	375(2)
6	^{85}Rb	422.2	17	34.6(1)	427(3)	0(1)	425(1)
51	^{85}Rb	422.2	17	31.6(2)	412(8)	6(2)	389(2)

dataset	isotope	B_0 / mT	T_0 / K	ΔB / μT	$\overline{\delta a_{\mathrm{HFS}}}$ / ppm	$\overline{\delta g_{\mathrm{J}}}$ / ppm	δa_{HFS} / ppm
75	^{85}Rb	422.2	17	33.9(7)	428(5)	2(1)	417(9)
52	^{85}Rb	422.2	15	31.9(2)	416(18)	7(4)	392(2)
17	^{85}Rb	422.2	13	33.8(2)	443(10)	7(2)	415(2)
53	^{85}Rb	422.2	13	33.3(2)	432(7)	6(1)	409(3)
65	^{87}Rb	491.8	23	52.0(8)	399(12)	–	396(6)
66	^{87}Rb	491.8	20	54.0(3)	414(5)	1(3)	412(2)
67	^{87}Rb	491.8	17	55.6(2)	427(10)	1(7)	424(2)
79	^{87}Rb	491.8	17	55.8(2)	430(9)	1(6)	426(1)
68	^{87}Rb	491.8	14	57.3(2)	437(7)	1(5)	437(2)
69	^{87}Rb	491.8	12.5	58.0(11)	454(71)	–	443(8)

The obtained results are visualised in Fig. 3.9 and 3.10 and compared to the results of $\overline{\delta a_{\mathrm{HFS}}}$. It is evident that the values for δa_{HFS} at $B_0 = 337.9\,\mathrm{mT}$ and $B_0 = 378.1\,\mathrm{mT}$ in Fig. 3.9 are clearly higher and lower than those at different B_0. This can be explained by Fig. 3.6, where one can see that the on-droplet peaks and the atom peaks of those transitions lie so close together that they partially overlap. Even if the two peaks are scanned seperately, i.e. by using either the TiSaph or the diode laser during one scan, this leads to slightly different measurement conditions and therefore to higher uncertainties.
One can also see that the results for ^{85}Rb show larger fluctuations than that of ^{87}Rb. This is due to the fact that in Fig. 3.9 results of older measurements from 2008 are depicted together with new ones, while there are only new measurement data evaluated in Fig. 3.9. Small changes may therefore be due to adaptations of the apparatus, especially a change of the gradient of the magnetic field can not be excluded.
Taking this into account, one can state that the results for both the old and the new evaluation method agree well with each other. The small differences between the values for a single ESR line though, can be seen as the result of the line asymmetry resulting from the droplet size distribution.
It may therefore be reasonable in line shape simulations, to evaluate δa_{HFS} for lines where the Gaussian function matches the data points and to take this value for all lines where there is a mismatch.

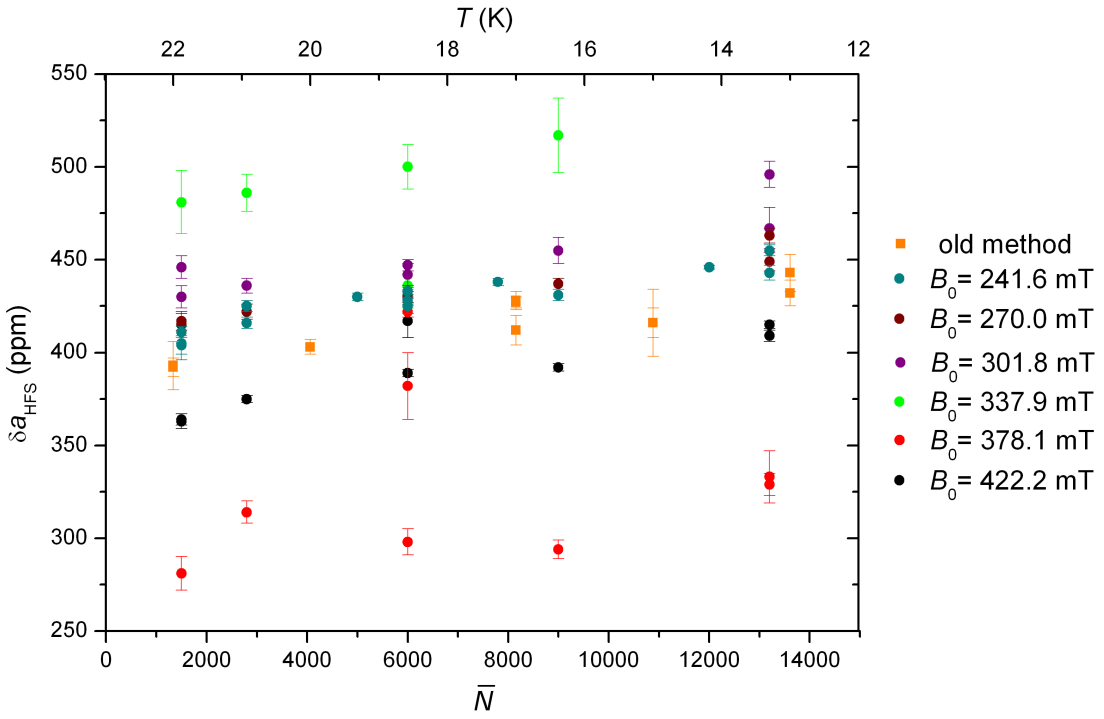

Figure 3.9.: Evaluation of δa_{HFS} for single (circles) ^{85}Rb ESR lines at different droplet sizes $\bar{N}$. Nozzle temperatures T_0 corresponding to the respective values of $\bar{N}$, are indicated at the top axis. To identify the ESR transition, the B_0-values of the free atom transitions are given. Also depicted are the results for $\overline{\delta a_{\mathrm{HFS}}}$ (squares), obtained by using the old evaluation method, i.e. variation of both, a_{HFS} and g_{J}.

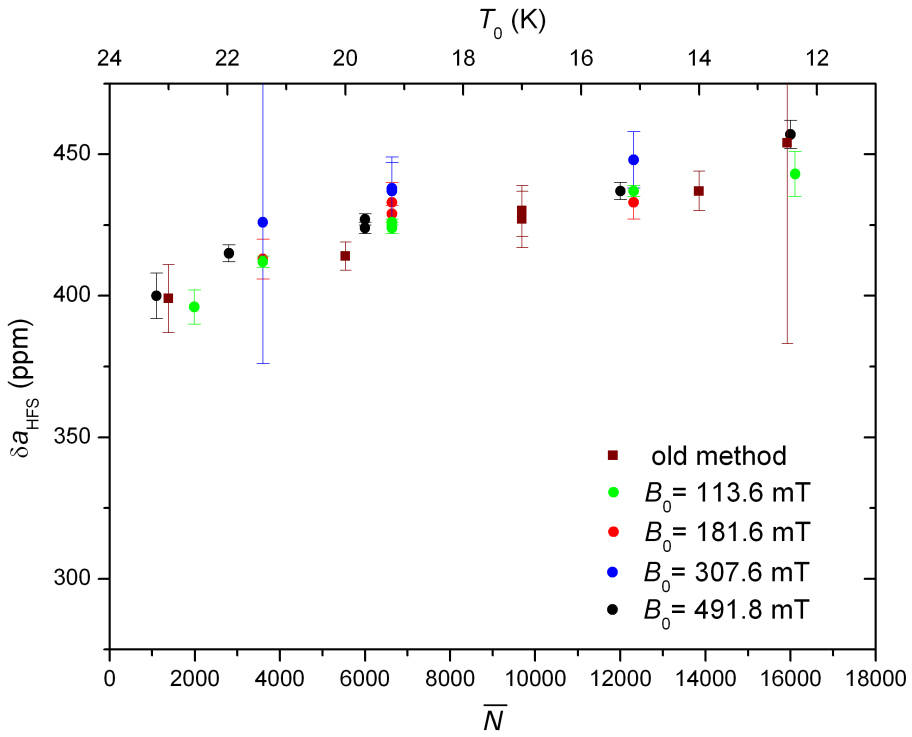

Figure 3.10.: Evaluation of δa_{HFS} for single (circles) ^{87}Rb ESR lines at different droplet sizes $\bar{N}$. Nozzle temperatures T_0 corresponding to the respective values of $\bar{N}$, are indicated at the top axis. To identify the ESR transition, the B_0-values of the free atom transitions are given. Also depicted are the results for $\overline{\delta a_{\mathrm{HFS}}}$ (squares), obtained by using the old evaluation method, i.e. variation of both, a_{HFS} and g_{J}.

Conclusion and Outlook

The method of ESR spectroscopy of single alkali-metal atoms attached to superfluid helium nanodroplets could be further improved in the course of this work. Higher sensitivity was obtained by investigation of ^{87}Rb ($a_{\mathrm{HFS}} \approx 3417\,\mathrm{MHz}$), leading to the publication of the first ESR spectra of this isotope [50]. The results concerning the change of the hyperfine constant δa_{HFS} were in good agreement with those of former experiments. However, the line intensities varied for different ESR transitions and showed a strong dependence on the laser polarization. On the basis of these results, a model for optical pumping of alkali-metal atoms on a helium droplets could be introduced and will be presented in the work of Johannes Poms [41].
Further on, the higher resolution brought up other new effects, especially the asymmetries of ESR line shapes, which are mainly a result of the helium droplet size distribution. In order to account for this fact, δa_{HFS} was evaluated for an extensive list of single ESR lines. The combination of the obtained results with detailed line shape analysis will be capable of predicting the droplet size distribution of $\mathrm{He_N}$ from ESR measurements for the first time.
The enhancement of the resolution is also a further step in the direction of spin labeling experiments, where ESR silent species shall be investigated by their interaction with alkali-metal atoms as spin labels. For this purpose, the simulation of the ESR lines may be necessary in order to detect small changes in ESR signals or line shapes. The results presented in this work will be a basis for these simulations.

A. Appendix

A.1. Calculations

A.1.1. Required Pressure in Vacuum Chambers

The mean free path $\bar{l}$ of a particle can be calculated using Eqn. 2.4:

$$\bar{l} = \frac{k_B \cdot T}{\sqrt{2}\pi p d^2}$$

With the help of this formula it is possible to calculate the vaccum pressure which has to be reached, so that $\bar{l}$ for a helium droplet is in the range of the length of the apparatus ($l \approx 1.7\,\mathrm{m}$):

$$p = \frac{k_B \cdot T}{\sqrt{2}\pi \bar{l} d^2}$$

$T = 293\,\mathrm{K}$ is the temperature of the residual gases in the chamber and k_B is the Boltzmann constant. The droplet diameter d can be calculated by help of Eqn. 1.5:

$$d = 2 \cdot R_0 = 2 \cdot 2.22 N^{\frac{1}{3}} \mathring{A}$$

With $N = 16000$ the mean number of helium atoms in a droplet at a nozzle temperature of 12.5 K (see Fig 3.2) one gets:

$$p = \frac{1.38 \cdot 10^{-23} \cdot 293}{\sqrt{2}\pi \left(2 \cdot 2.2 \cdot 16000^{1/3} \cdot 10^{-10}\right) \cdot 1.7} \approx 4.4 \cdot 10^{-6}\ \mathrm{Pa} = 4.4 \cdot 10^{-8}\ \mathrm{mbar}$$

Note that when the length of the apparatus l is equal to the mean free path, there is still a reasonable chance for a droplet to collide with other particles. In general one aims $\bar{l} \approx 10 \cdot l$, which can be reached by reducing p one order of magnitude further.

A.1.2. Estimation of Liquid Nitrogen Consumption in Cryo Pump

The following calculation shall result in an estimate for the minimum time that the cryo pump can work without any refill of additional liquid nitrogen.
Two cylinders with an inner diameter d of 6 cm and a length l of 30 cm form the reservoir of the cryo pump (the volume of the connection piece is neglected). The volume of these

cylinders corresponds to the maximum amount of liquid nitrogen in the reservoir.

$$\begin{aligned} V &= \frac{d^2\pi}{4} \cdot l \\ V &= \underbrace{2}_{\text{cylinders}} \cdot \frac{6^2\pi}{4} \cdot 30 \approx 1700 \text{ cm}^3 = 1.7 \text{ l} \end{aligned} \tag{A.1}$$

The mass density of liquid nitrogen and the heat of vaporization are 804 g/l and $199.2 \cdot 10^3$ J/kg [35]. Evaporation of all liquid N_2 in the reservoir therefore needs a total heat transfer to the cryo pump of approx. 272 kJ.
This heat transfer can take place by convection, thermal conduction and radiation. As the reservoir of the cryo pump is situated inside the pickup chamber, convection can be neglected. Further on, the only thermal contact between the cryo pump and the wall of the vacuum chamber is realised via the PTFE sealings of the two fixation flanges. The poor thermal conduction of PTFE (0.259 W/(mK) see Ref. [42]) in combination with the small area of the sealings leads to neglection of this part of the heat transfer.
For the radiative heat transfer $\dot{Q}$ from the chamber walls to the cryo pump one gets in accordance to Ref. [22]

$$\dot{Q} = \epsilon \cdot \sigma \cdot A \cdot \left(T_{\text{cw}}^4 - T_{\text{cp}}^4\right) \tag{A.2}$$

Here ϵ is the emissivity, which is 1 for a black body and < 1 for grey bodies. For simplifaction ϵ is set to 1. The Stefan- Boltzman constant σ is $5.67 \cdot 10^{-8}$ W/(m^{2}K^4) and the area A of the two cylinder barrels can be calculated to be approx. 0.11 m^2. T_{cw} and T_{cp} are the temperatures of the chamber wall (300 K) and of the surface of the cryo pump (77 K when filled with liquid N_2). Inserting all this values in Eqn. A.2 leads to

$$\dot{Q} \approx 50 \text{ W}$$

The total operation time t without any refill of liquid N_2 is

$$t = \tfrac{272 \cdot 10^3}{50} = 5440 \text{ s} \approx 1.5 \text{ hrs}$$

which is in good agreement with accomplished tests.

B. Appendix

B.1. CD Content

- Drawings
  - AutoCAD drawings of cryo pump
- Matlab programs
  - folder ga_Simulations: several programs to evaluate δa_{HFS} (see Sec. 3.1)
  - folder Fitprogrames: several programs to evaluate the ESR line shift for full sets of ESR lines
  - folder AHFS-change: several programs to evaluate δa_{HFS} for constant g_{J} (see Sec. 3.2)
- Origin files
  - evaluation of δa_{HFS} for single ESR lines (graphics)
  - influence of laser polarization on ESR signals– optical pumping (see Sec. 3.1)
  - pressure and temperature evolutions during bake out process
- Lyx files
  - tables of ESR measurements overview and evaluation of single ESR lines (see Sec. 3.2 and B.2)
- Raw data
- Thesis

B.2. Measurement Overview

Table B.1.: Overview of ESR datasets collected for ^{85}Rb and ^{87}Rb. Data taken before 11.11.2010 has already been published in Ref. [27], but is itemised once again in more detail. The numbering in the column *dataset* corresponds to the denotation of lines in Tab. REFERENZ. m_I labels the respective ESR transitions and B_0 is the magnetic field where these transitions occur for the free atoms for a MW- frequency of ≈ 9442 MHz.

isotope	date	data files (ESRxxxx.txt)	what was measured	m_I	B_0 / mT	dataset
^{85}Rb	17.11.2008	1279-1282	HFS spectrum, $T_0 = 17\,\mathrm{K}$ / $p_0 = 50\,\mathrm{bar}$	-5/2	241.6	1
		1271-1275		-3/2	270.0	2
		1234-1240		-1/2	301.8	3
		1244-1248		+1/2	337.9	4
		1251-1254		+3/2	378.1	5
		1262-1265/1267-1268		+5/2	422.2	6
^{85}Rb	03.12.2008	1353-1355	T_0-scan, $T_0 = 22\,\mathrm{K}$ / $p_0 = 50\,\mathrm{bar}$	-5/2	241.6	7
		1361-1363	$T_0 = 20\,\mathrm{K}$			8
		1364-1366	$T_0 = 18\,\mathrm{K}$			9
		1367-1369	$T_0 = 16\,\mathrm{K}$			10
		1372-1374	$T_0 = 14\,\mathrm{K}$			11
^{85}Rb	17.12.2008	1491	HFS spectrum, $T_0 = 13\,\mathrm{K}$ / $p_0 = 50\,\mathrm{bar}$	-5/2	241.6	12
		1493		-3/2	270.0	13
		1497		-1/2	301.8	14
		1499-1500	seperate scans over free- and atom peak	+1/2	337.9	15
		1507-1508		+3/2	378.1	16
		1511		+5/2	422.2	17
		1514	HFS spectrum, $T_0 = 22\,\mathrm{K}$ / $p_0 = 50\,\mathrm{bar}$	-5/2	241.6	18
		1516		-3/2	270.0	19
		1520		-1/2	301.8	20
		1522-1524		+1/2	337.9	21

isotope	date	data files (ESRxxxx.txt)	what was measured	m_I	B_0 / mT	dataset
^{85}Rb	17.12.2008	1527-1528	HFS spectrum, $T_0 = 22\,\mathrm{K}$ / $p_0 = 50\,\mathrm{bar}$	+3/2	378.1	22
		1530-1531		+5/2	422.2	23
		1581	T_0-scan, $T_0 = 22\,\mathrm{K}$ / $p_0 = 50\,\mathrm{bar}$	-5/2	241.6	24
		1582	$T_0 = 20\,\mathrm{K}$			25
		1583	$T_0 = 17\,\mathrm{K}$			26
		1584	$T_0 = 15\,\mathrm{K}$			27
		1585	$T_0 = 13\,\mathrm{K}$			28
		1569	T_0-scan, $T_0 = 22\,\mathrm{K}$ / $p_0 = 50\,\mathrm{bar}$	-3/2	270.0	29
		1570	$T_0 = 20\,\mathrm{K}$			30
		1571	$T_0 = 17\,\mathrm{K}$			31
		1572	$T_0 = 15\,\mathrm{K}$			32
		1573	$T_0 = 13\,\mathrm{K}$			33
		1561	T_0-scan, $T_0 = 22\,\mathrm{K}$ / $p_0 = 50\,\mathrm{bar}$	-1/2	301.8	34
		1562	$T_0 = 20\,\mathrm{K}$			35
		1563	$T_0 = 17\,\mathrm{K}$			36
		1564	$T_0 = 15\,\mathrm{K}$			37
		1565	$T_0 = 13\,\mathrm{K}$			38
		1551	T_0-scan, $T_0 = 22\,\mathrm{K}$ / $p_0 = 50\,\mathrm{bar}$	+1/2	337.9	39
		1552-1553	$T_0 = 20\,\mathrm{K}$			40
		1554	$T_0 = 17\,\mathrm{K}$			41
		1555	$T_0 = 15\,\mathrm{K}$			42
		1556	$T_0 = 13\,\mathrm{K}$			43
		1540/1543	T_0-scan, $T_0 = 22\,\mathrm{K}$ / $p_0 = 50\,\mathrm{bar}$	+3/2	378.1	44
		1544	$T_0 = 20\,\mathrm{K}$			45
		1545-1546	$T_0 = 17\,\mathrm{K}$			46
		1547-1548	$T_0 = 15\,\mathrm{K}$			47
		1549	$T_0 = 13\,\mathrm{K}$			48

isotope	date	data files (ESRxxxx.txt)	what was measured	m_I	B_0 / mT	dataset
^{85}Rb	17.12.2008	1533	T_0-scan, $T_0 = 22\,\mathrm{K}$ / $p_0 = 50\,\mathrm{bar}$	+5/2	422.2	49
		1534	$T_0 = 20\,\mathrm{K}$	+5/2	422.2	50
		1535	$T_0 = 17\,\mathrm{K}$			51
		1536	$T_0 = 15\,\mathrm{K}$			52
		1537	$T_0 = 13\,\mathrm{K}$			53
^{87}Rb	11.11.2010	3404-3406	T_0-scan, $T_0 = 23\,\mathrm{K}$ / $p_0 = 50\,\mathrm{bar}$	+3/2	113.6	54
		3400-3402	$T_0 = 20\,\mathrm{K}$			55
		3396/3398-3399	$T_0 = 17\,\mathrm{K}$			56
		3407-3409	$T_0 = 14\,\mathrm{K}$			57
		3411-3413	$T_0 = 12.5\,\mathrm{K}$			58
		3376-3377/3379-3381	T_0-scan, $T_0 = 20\,\mathrm{K}$ / $p_0 = 50\,\mathrm{bar}$	+1/2	181.6	59
		3365-3369	$T_0 = 17\,\mathrm{K}$			60
		3385-3386/3389-3390	$T_0 = 14\,\mathrm{K}$			61
		3427-3428	T_0-scan, $T_0 = 20\,\mathrm{K}$ / $p_0 = 50\,\mathrm{bar}$	-1/2	307.6	62
		3422-3425	$T_0 = 17\,\mathrm{K}$			63
		3436/3438-3440	$T_0 = 14\,\mathrm{K}$			64
		3455	T_0-scan, $T_0 = 23\,\mathrm{K}$ / $p_0 = 50\,\mathrm{bar}$	-3/2	491.8	65
		3453-3454	$T_0 = 20\,\mathrm{K}$			66
		3450/3452	$T_0 = 17\,\mathrm{K}$			67
		3445/3448	$T_0 = 14\,\mathrm{K}$			68
		3460	$T_0 = 12.5\,\mathrm{K}$			69
^{85}Rb	22.11.2010	3537-3538	HFS spectrum, $T_0 = 17\,\mathrm{K}$ / $p_0 = 50\,\mathrm{bar}$	-5/2	241.6	70
		3543-3544		-3/2	270.0	71
		3551-3552		-1/2	301.8	72
		3576-3577	seperate scans over free- and atom peak	+1/2	337.9	73
		3586-3587		+3/2	378.1	74
		3603-3604		+5/2	422.2	75

isotope	date	data files (ESRxxxx.txt)	what was measured	m_I	B_0 / mT	dataset
^{87}Rb	22.11.2010	3510/3513/3517	HFS spectrum, $T_0 = 17\,\mathrm{K}$ / $p_0 = 50\,\mathrm{bar}$	+3/2	113.6	76
		3527-3529		+1/2	181.6	77
		3564/3566-3567		-1/2	307.6	78
		3615-3616		-3/2	491.8	79
^{87}Rb	24.03.2011	4115-4120/4123-4126	T_0-scan, $T_0 = 20\,\mathrm{K}$ / $p_0 = 50\,\mathrm{bar}$	+3/2	113.6	80
		4076/4079/4081/4084-4086	$T_0 = 17\,\mathrm{K}$			81
		4087-4088/4091-4094	$T_0 = 15\,\mathrm{K}$	+3/2	113.6	82
		4095-4100	$T_0 = 13.5\,\mathrm{K}$			83
^{87}Rb	13.04.2011	4186-4190	p_0-scan, $p_0 = 30\,\mathrm{bar}$ / $T_0 = 17\,\mathrm{K}$	+3/2	113.6	84
		4137-4143	$p_0 = 40\,\mathrm{bar}$			85
		4144-4148	$p_0 = 50\,\mathrm{bar}$			86
		4150-4154	$p_0 = 60\,\mathrm{bar}$			87
		4155-4159	$p_0 = 70\,\mathrm{bar}$			88
		4160-4164	$p_0 = 80\,\mathrm{bar}$			89
		4166-4171	$p_0 = 90\,\mathrm{bar}$			90
		4172-4176	$p_0 = 100\,\mathrm{bar}$			91
		4177-4178	$p_0 = 110\,\mathrm{bar}$			92
		4192-4196	p_0-scan, $p_0 = 40\,\mathrm{bar}$ / $T_0 = 20\,\mathrm{K}$	+3/2	113.6	93
		4198-4202	$p_0 = 50\,\mathrm{bar}$			94
		4205-4209	$p_0 = 60\,\mathrm{bar}$			95
		4210-4214	$p_0 = 70\,\mathrm{bar}$			96
		4215-4219	$p_0 = 80\,\mathrm{bar}$			97
		4220-4224	$p_0 = 90\,\mathrm{bar}$			98
		4225-4229	$p_0 = 100\,\mathrm{bar}$			99
		4230-4232	$p_0 = 110\,\mathrm{bar}$			100
			Xe added / $p_0 = 80\,\mathrm{bar}$ / $T_0 = 17\,\mathrm{K}$	+3/2	113.6	
		4236-4238	0 turns			101

isotope	date	data files (ESRxxxx.txt)	what was measured	m_I	B_0 / mT	dataset
^{87}Rb	13.04.2011		Xe added / $p_0 = 80\,\mathrm{bar}$ / $T_0 = 17\,\mathrm{K}$	$+3/2$	113.6	
		4239-4242	3.25 turns			102
		4243-4247	3.50 turns			103
		4248-4252	3.75 turns			104
		4256-4262	4.00 turns			105
			He added / $p_0 = 80\,\mathrm{bar}$ / $T_0 = 17\,\mathrm{K}$	$+3/2$	113.6	
		4265-4272	4.00 turns			106

C. Appendix

C.1. Drawings

In this chapter the CAD drawings of the cooling trap are given in 2D and 3D, as well as a depiction of the traps's position inside the pickup chamber (drawing of the chamber taken from Ref. [32]).
All dimensions are given in mm. Note that the prints are not exact to scale.

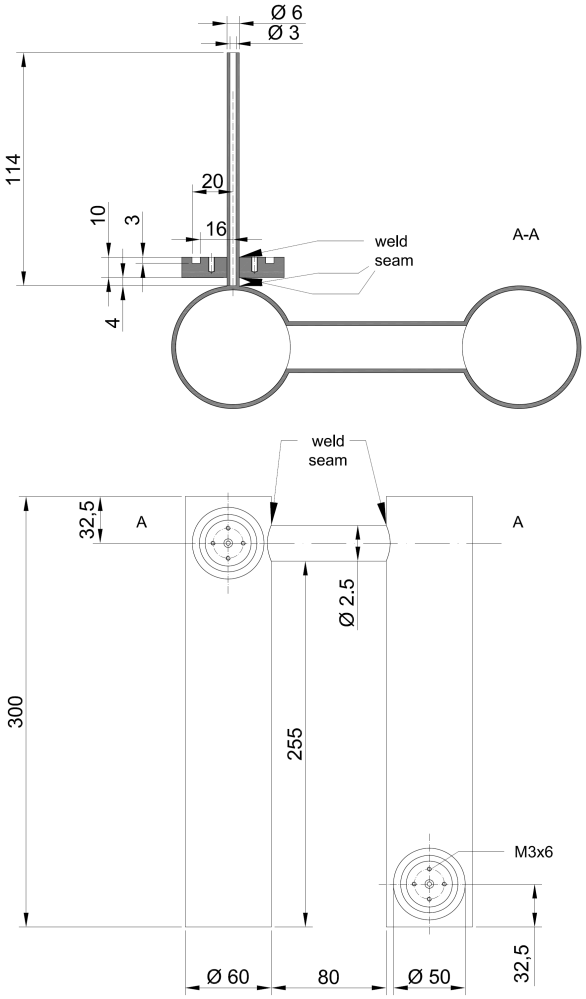

1 Piece				Material: high quality steel	

	Date	Name
Editor	2011	Volk

Scale 1:4

cryo pump

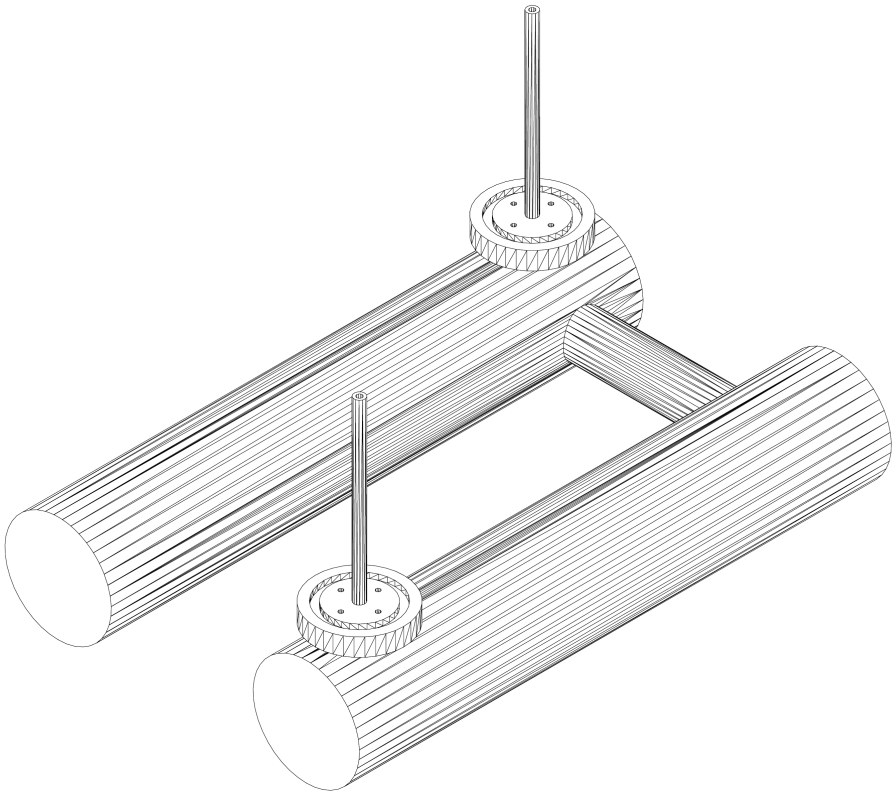

1 Piece				Material: high quality steel	

	Date	Name
Editor	2011	Volk

Scale 1:4	cryo pump 3D

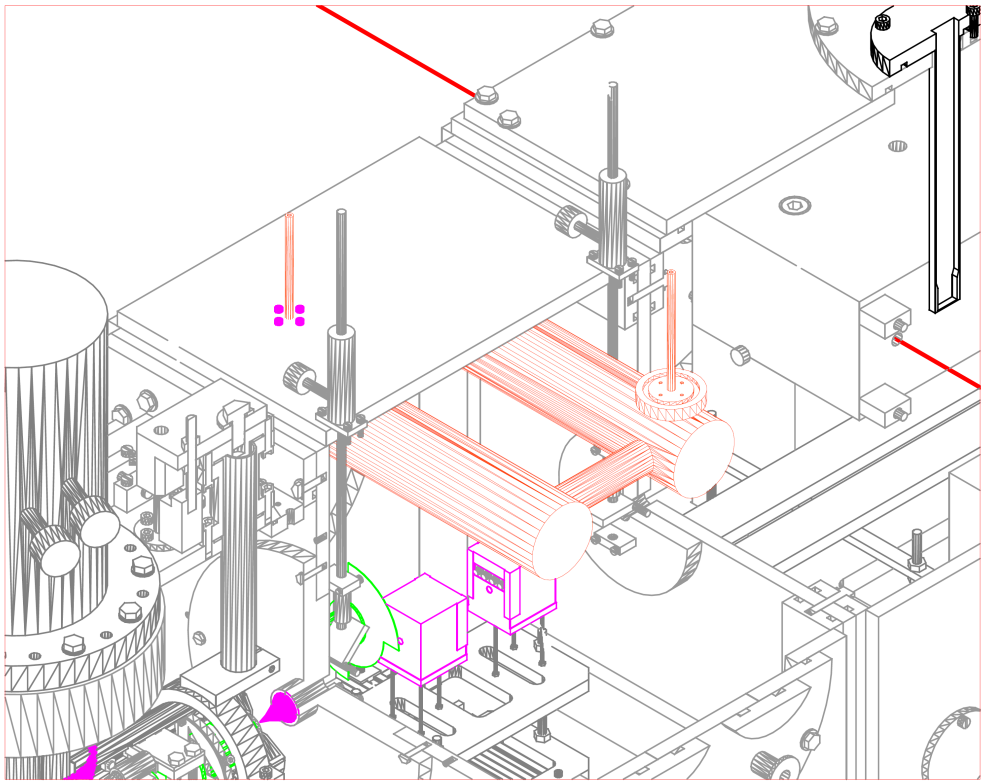

Piece	Name	Material	No.		
	Dat.	Name			
Editor	2011				
Scale.	cryo pump position				

Bibliography

[1] F. Ancilotto, E. Cheng, M. W. Cole, and F. Toigo. The binding of alkali atoms to the surfaces of liquid-helium and hydrogen. *Zeitschrift für Physik B–Condensed Matter*, 98(3):323–329, Sept. 1995.

[2] V. A. Apkarian and N. Schwentner. Molecular photodynamics in rare gas solids. *Chemical Reviews*, 99(6):1481–1514, June 1999.

[3] E. Arimondo, M. Inguscio, and P. Violino. Experimental determinations of hyperfine-structure in alkali atoms. *Reviews Of Modern Physics*, 49(1):31–75, 1977.

[4] P. W. Atkins and J. de Paula. *Physical Chemistry*. Oxford University Press, 2006. ISBN 0198700725. 1064 pp.

[5] G. Auböck, J. Nagl, C. Callegari, and W. E. Ernst. Electron spin pumping of Rb atoms on He nanodroplets via nondestructive optical excitation. *Physical Review Letters*, 101(3):035301–1–4, July 2008.

[6] E. W. Becker, R. Klingelhofer, and P. Lohse. Strahlen aus Kondensiertem Helium im Hochvakuum. *Zeitschrift für Naturforschung Part A–Astrophysik Physik und Physikalische Chemie*, 16(11):1259–1259, 1961.

[7] G. Breit and I. I. Rabi. Measurement of nuclear spin. *Physical Review*, 38(11):2082–, Dec. 1931.

[8] F. Bruehl, R. Trasca, and W. E. Ernst. Rb-He exciplex formation on helium nanodroplets. *Journal of Chemical Physics*, 115(22):10220–10224, 2001. cited By (since 1996) 39.

[9] H. Buchenau, E. L. Knuth, J. Northby, J. P. Toennies, and C. Winkler. Mass spectra and time-of-flight distributions of helium cluster beams. *Journal of Chemical Physics*, 92(11):6875–6889, June 1990.

[10] C. Callegari and W. E. Ernst. Helium nanodroplets. In F. Merkt and M. Quack, editors, *Handbook of High Resolution Spectroscopy*. Wiley, 2011.

[11] C. Callegari, J. Higgins, F. Stienkemeier, and G. Scoles. Beam depletion spectroscopy of alkali atoms (Li, Na, K) attached to highly quantum clusters. *The Journal of Physical Chemistry A*, 102(1):95–101, 1998.

[12] W. J. Childs. Overview of laser-radiofrequency double-resonance studies of atomic, molecular, and ionic beams. *Physics Reports*, 211(3):113–165, Feb. 1992.

[13] F. Dalfovo. Atomic and molecular impurities in ^{4}He clusters. *Zeitschrift für Physik D–Atoms Molecules and Clusters*, 29(1):61–66, Jan. 1994.

[14] W. Demtröder. *Laser Spectroscopy: Basic Concepts and Instrumentation*. Springer, Berlin Heidelberg, 1998. ISBN 354057171X. 924 pp.

[15] W. E. Ernst, S. Kindt, and T. Törring. Precise Stark-effect measurements in the $^2\Sigma$ ground state of CaCl. *Physical Review Letters*, 51(11):979–981, Sept. 1983.

[16] T. E. Gough, M. Mengel, P. A. Rowntree, and G. Scoles. Infrared-spectroscopy at the surface of clusters - SF_6 on Ar. *Journal of Chemical Physics*, 83(10):4958–4961, 1985.

[17] H. Haken and H. C. Wolf. *Atom- und Quantenphysik*. Springer, 8 edition, 2003. ISBN 3540026215.

[18] W. Happer. Optical-pumping. *Reviews of Modern Physics*, 44(2):169–249, 1972.

[19] J. Harms, M. Hartmann, J. P. Toennies, A. F. Vilesov, and B. Sartakov. Rotational structure of the IR spectra of single SF_6 molecules in liquid He-3 and He-3 droplets. *Journal of Molecular Spectroscopy*, 185(1):204–206, Sept. 1997.

[20] J. Harms, J. P. Toennies, and F. Dalfovo. Density of superfluid helium droplets. *Physical Review B*, 58(6):3341–3350, Aug. 1998.

[21] I. V. Hertel and C.-P. Schulz. *Atome, Moleküle und optische Physik 1*. Springer, 2008.

[22] W. Jitschin. *Wutz Handbuch Vakuumtechnik*, volume 10. Vieweg + Teubner, 2010. 912 pp.

[23] G. Kirchhoff and R. Bunsen. Chemische Analyse durch Spectralbeobachtungen. *Annalen der Physik und Chemie*, 110:161–189, 1860.

[24] E. L. Knuth. Size correlations for condensation clusters produced in free-jet expansions. *Journal of Chemical Physics*, 107(21):9125–9132, Dec. 1997.

[25] E. L. Knuth and U. Henne. Average size and size distribution of large droplets produced in a free-jet expansion of a liquid. *Journal of Chemical Physics*, 110(5): 2664–2668, Feb. 1999.

[26] E. L. Knuth, B. Schilling, and T. J. Peter. *On Scaling Parameters for Predicting Cluster Sizes in Free Jets*, volume 1 of *Rarefied Gas Dynamics*. Oxford University Press, Oxford, 1995. 270 pp.

[27] M. Koch. *Magnetic Resonance Spectroscopy of Single Alkali-Metal Atoms Isolated in Superfluid Helium Nanodroplets*. PhD thesis, Graz University of Technology, 2009.

[28] M. Koch, G. Auböck, C. Callegari, and W. E. Ernst. Coherent spin manipulation and ESR on superfluid helium nanodroplets. *Physical Review Letters*, 103(3):035302–1–4, July 2009.

[29] M. Koch, C. Callegari, and W. E. Ernst. Alkali-metal electron spin density shift induced by a helium nanodroplet. *Molecular Physics: An International Journal at the Interface Between Chemistry and Physics*, 108(7):1005–1011, 2010.

[30] M. Koch, J. Lanzersdorfer, C. Callegari, J. S. Muenter, and W. E. Ernst. Molecular beam magnetic resonance in doped helium nanodroplets. A setup for optically detected ESR/NMR in the presence of unresolved Zeeman splittings. *The Journal of Physical Chemistry A*, 113(47):13347–13356, Nov. 2009.

[31] P. Kusch, S. Millman, and I. I. Rabi. The radiofrequency spectra of atoms hyperfine structure and Zeeman effect in the ground state of Li-6, Li-7, K-39 and K-41. *Physical Review*, 57(9):765–780, May 1940.

[32] J. Lanzersdorfer. Assembly and test of a helium cluster beam apparatus for magnetic field studies of atom and molecule doped helium nanodroplets. Master's thesis, Institute of Experimental Physics, Graz University of Technology, 2008.

[33] M. Lewerenz, B. Schilling, and J. P. Toennies. A new scattering deflection method for determining and selecting the sizes of large liquid clusters of ^{4}He. *Chemical Physics Letters*, 206(1-4):381–387, Apr. 1993.

[34] M. Lewerenz, B. Schilling, and J. P. Toennies. Successive capture and coagulation of atoms and molecules to small clusters in large liquid helium clusters. *Journal of Chemical Physics*, 102(20):8191–8207, May 1995.

[35] D. R. Lide, editor. *CRC Handbook of Chemistry and Physics*. CRC Press, Boca Raton, FL, 77th edition, 1996. ISBN 0849304776.

[36] R. D. McCarty. Thermodynamic properties of helium 4 from 2 to 1500 K at pressures to 10^8 Pa. *Journal of Physical and Chemical Reference Data*, 2(4):923–1042, 1973.

[37] D. R. Miller. *Atomic and Molecular Beam Methods 1*, volume 1. Oxford University Press, New York, USA, 1988. ISBN ISBN 0195042808. 752 pp.

[38] J. Nagl, G. Auböck, C. Callegari, and W. E. Ernst. Magnetic dichroism of potassium atoms on the surface of helium nanodroplets. *Physical Review Letters*, 98(7):075301–1–4, Feb. 2007.

[39] J. Nagl, G. Auböck, A. W. Hauser, O. Allard, C. Callegari, and W. E. Ernst. High-spin alkali trimers on helium nanodroplets: Spectral separation and analysis. *Journal of Chemical Physics*, 128(15):154320–1–8, Apr. 2008.

[40] H. Pauly. *Atom, Molecule and Cluster Beams I: Basic Theory, Production and Detection of Thermal Energy Beams.* Springer Series in Atomic, Molecular, Optical, and Plasma Physics. Springer, Berlin, 2000. ISBN I3540669450. 344 pp.

[41] J. Poms. Optical detection of ESR on doped helium droplets: the influence of optical pumping in experiment and theory. Master's thesis, Institute of Experimental Physics, Graz University of Technology, will be published 2011.

[42] M. Price and M. Jarratt. Thermal conductivity of PTFE and PTFE composites. *Thermochimica Acta*, 392-393:231–236, September 2002.

[43] I. I. Rabi, S. Millman, P. Kusch, and J. R. Zacharias. The molecular beam resonance method for measuring nuclear magnetic moments. *Physical Review*, 55(6):526–, Mar. 1939.

[44] I. I. Rabi, J. R. Zacharias, S. Millman, and P. Kusch. A new method of measuring nuclear magnetic moment. *Physical Review*, 53(4):318, Feb. 1938.

[45] Y. Ralchenko, A. Kramida, J. Reader, and NIST ASD Team. NIST atomic spectra database, v. 4.0.1, http://physics.nist.gov/asd. online, Mar. 2011.

[46] M. Ratschek. Doping helium droplets: development of a high temperature pickup source. Master's thesis, Institute of Experimental Physics, Graz University of Technology, 2010.

[47] M. Ratschek, M. Koch, and W. E. Ernst. Electron-bombardment evaporation for doping superfluid helium nanodroplets with Cr atoms and Cr clusters. in preparation.

[48] J. P. Toennies and A. F. Vilesov. Spectroscopy of atoms and molecules in liquid helium. *Annual Review of Physical Chemistry*, 49:1–41, 1998.

[49] J. P. Toennies and A. F. Vilesov. Superfluid helium droplets: a uniquely cold nanomatrix for molecules and molecular complexes. *Angewandte Chemie-International Edition*, 43(20):2622–2648, 2004.

[50] A. Volk, J. Poms, M. Koch, and W. Ernst. ^{87}Rb Electron Spin Resonance on Helium Nanodroplets: The Influence of Optical Pumping. *The Journal of Physical Chemistry A*, in press 2011.

[51] S. Vongehr and V. V. Kresin. Unusual pickup statistics of high-spin alkali agglomerates on helium nanodroplets. *Journal of Chemical Physics*, 119(21):11124–11129, Dec. 2003.

[52] J. A. Weil, J. R. Bolton, and J. E. Wertz. *Electron Paramagnetic Resonance: Elementary Theory and Practical Applications*. John Wiley & Sons, 1994. ISBN 0471572349. 592 pp.

[53] E. Zavoisky. The paramagnetic absorption of a solution in parallel fields. *Journal of Physics-ussr*, 8(1-6):377–380, 1944.